Materials Science & Engineering C 115 (2020) 111130

Contents lists available at ScienceDirect

Materials Science & Engineering C

journal homepage: www.elsevier.com/locate/msec

The effects of severe plastic deformation on the mechanical and corrosion characteristics of a bioresorbable Mg-ZKQX6000 alloy

M.W. Vaughan[a], A.I. Karayan[a], A. Srivastava[a], B. Mansoor[a,b,*], J.M. Seitz[c], R. Eifler[c], I. Karaman[a], H. Castaneda[a], H.J. Maier[c]

[a] Department of Materials Science and Engineering, Texas A&M University, College Station, TX, USA
[b] Mechanical Engineering Program, Texas A&M University at Qatar, Doha, Qatar
[c] Institut für Werkstoffkunde (IW), Leibniz Universität Hannover, An der Universität 2, 30823 Hannover, Germany

ARTICLE INFO

Keywords:
Magnesium
Bioresorbable orthopedic implants
Severe plastic deformation
Equal channel angular pressing
Anodic dissolution
Corrosion

ABSTRACT

In this work, a bioresorbable Mg-ZKQX6000 (Mg–6Zn–0.6Zr–0.4Ag–0.2Ca (wt%)) alloy was severely plastically deformed via equal channel angular pressing (ECAP) according to three unique hybrid routes at low temperatures (200 °C to 125 °C). The roles of ECAP processing on microstructure, and ensuing mechanical properties and corrosion rates, are assessed. Microstructurally, ECAP induces a complex plethora of features, especially variations in grain sizes and precipitates' sizes, distributions, and morphologies for individual cases. Mechanically, ECAP generally refined grain size, resulting in ultra-high strength levels of about 400 MPa in ultimate tensile strength for several cases; however, deformation via ECAP of precipitates induced embrittlement and low elongation to failure levels. Corrosion testing, conducted in simulated bodily fluid at bodily pH levels to mimic conditions in the human body, revealed consistent corrosion rates across several techniques (mass loss, hydrogen evolution, and electrochemical impedance spectroscopy (EIS)), showing that severe plastic deformation deteriorates corrosion resistance for this material. In-situ corrosion monitoring explained that corrosion accelerated after ECAP due to the creation of heterogeneous, anodic shear zones, which exhibited dense regions of refined grains and fine precipitates. Suggestions for future design and thermomechanical processing of Mg alloys for bioresorbable orthopedic implants are provided.

1. Introduction

In recent years, magnesium alloys have received considerable attention as structural materials for weight-critical applications, owing to magnesium's inherent low density (1.74 g/cm^3) and high specific strength in comparison to conventional steels and aluminum alloys [1–3]. As Mg and its alloys are roughly 25% the density of steels and 66% the density of Al alloys, they are currently being used for lightweighting in a variety of industries; some examples include the transportation industry for energy conservation [4,5], the defense sector for lightweight armor [6], and the electronics industry for personal devices [7]. As most commercial Mg alloys were originally developed for weight-sensitive applications, their designs strongly emphasized enhanced strength, formability, and corrosion resistance [2,4,8,9]. However, dramatic improvements in said properties via alloying are often inhibited because many alloying elements exhibit low solubility in magnesium [10]. For instance, there is no element sufficiently soluble in magnesium to form a protective oxide layer on the surface, as Cr does when added to Fe in stainless steels [11].

Presently, significant efforts are developing magnesium alloys for use in the medical field for temporary, bioresorbable implants [12–16]. Inherently, magnesium is a highly reactive metal and exhibits a rapid corrosion rate, especially in chloride containing solutions [4,5], such as physiological environments. Briefly, Mg corrosion in aqueous environments occurs by the following half-cell reactions [17]:

$$Mg \rightarrow Mg^{2+} + 2e^- \quad (1)$$

$$2H_2O + 2e^- \rightarrow 2OH^- + H_2\,(g) \quad (2)$$

where, as one mole of Mg yields one mole of hydrogen gas, theoretically the mass loss rate of Mg during immersion in aqueous media can be checked against the rate of evolved H_2 gas [18,19]. Eqs. (1) and (2) also demonstrate that a rapid corrosion rate of Mg can have the adverse effect of producing high levels of evolved hydrogen gas in the body, which can be toxic to the physiological environment.

Despite these challenges, magnesium itself, already abundantly

* Corresponding author at: Department of Materials Science and Engineering, Texas A&M University, College Station, TX, USA.
E-mail address: bilal.mansoor@qatar.tamu.edu (B. Mansoor).

https://doi.org/10.1016/j.msec.2020.111130
Received 12 February 2020; Received in revised form 7 April 2020; Accepted 26 May 2020
Available online 28 May 2020

present in the body, exhibits excellent biocompatibility [12,20] and possesses similar mechanical properties to cortical bone, such as density and elastic modulus [7,14,16,21]. Coupling this, then, with its rapid corrosion rate in vivo makes Mg alloys promising material candidates for temporary (i.e. bioresorbable) orthopedic implants, provided the corrosion rate can be adequately controlled [12,13]. In orthopedics, bioresorbable implants eliminate long-term side-effects, such as stress shielding, associated with biologically inert implants, which often require further treatment and surgeries, and induce trauma and add expense for the patient [12,16]. In the ideal case, Mg orthopedic implants would provide the patient with sufficient mechanical support and functionality, while safely and gradually being resorbed into the body and replaced by healed bone tissue [20].

It is well known that alloying and thermomechanical processing determine mechanical properties and corrosion rates in Mg alloys. Regarding alloying and corrosion rates, elements such as Zn and Al, when alloyed with magnesium, promote less negative corrosion potentials, indicating lower tendencies for corrosion; other alloying elements, such as rare earths, can show the opposite effect [22]. For biomedical implants, alloying should be generally restricted to biocompatible elements, although elemental dissolution rate, which may be compared with the human body's maximum daily allowable dosage, is perhaps a more accurate measure of potential toxicity and must be considered for all alloying elements [12,20]. As mentioned, even Mg itself can pose a health risk if it corrodes too quickly, due to the release of hydrogen gas into the system (Eq. (2)). Also, some elements, such as Al, should be completely avoided; Al is cytotoxic and linked to Alzheimer's disease [14,15]. After alloying elements and their amounts have been selected, the Mg alloy's microstructural features – a product of the thermomechanical processing – will largely determine mechanical properties and corrosion rates. It is important to promote excellent mechanical properties in addition to a controlled and moderate corrosion rate, for, in vivo, an orthopedic implant's integrity – and hence mechanical properties such as strength – reduce with time due to corrosion.

With these ideas in mind, a complex balancing act of corrosion rate versus mechanical properties exists in the development of a Mg alloy with the proper functionality for bioresorbable orthopedic implants. While microstructural features such as precipitates, grain size, and crystallographic texture have well-known effects on mechanical properties of magnesium alloys [2,3,8,9,23–26], the effects of these factors on corrosion properties are less established. Among them, precipitates are known to be particularly influential on corrosion rate, as they may be either anodic or cathodic to the Mg matrix and thereby complete the electrochemical cell in the presence of an electrolyte [27]. This results in micro-galvanic coupling, i.e. anodic dissolution. In Mg alloys, effects of precipitate chemistry, size, morphology, and distribution on corrosion vary and are poorly understood. Studies on the corrosion behavior of fine-grained Mg alloys with or without precipitates have reported conflicting findings of reduced [5,11,28–31] or increased [25,32–35] corrosion rates with grain refinement for pure magnesium and a variety of magnesium alloys, including AZ31, AZ61, ZK60, and AZ91D, where precipitate refinement often occurs simultaneously with grain refinement during processing. The difficulty in ascertaining the effects of precipitates on corrosion rate has led some to suggest that a connected distribution of cathodic precipitates may allow for *improved* corrosion resistance by serving as a protective barrier to the anodic phase (i.e. Mg matrix) [4,19]. It is also worth mentioning that the effects of texture on corrosion rate for magnesium alloys are not well understood, although the general consensus is that basal planes, when exposed to an electrolyte, provide enhanced corrosion resistance in comparison to other planes [36,37]. The reasoning here is that basal planes are the least thermodynamically reactive plane in Mg, possessing the highest binding energy and lowest surface energy [5].

In light of the aforementioned challenges facing bioresorbable orthopedic implants made from Mg alloys, the purpose of this paper is two-fold. The first goal of this work is to explore the strengthening potential of a high-strength, bioresorbable Mg alloy, in the interest of orthopedic implant applications; the second goal is to understand the effects of strengthening on both microstructure – especially precipitate distribution, morphology, and size – and the resulting corrosion rates in a simulated physiological environment. In this effort, the composition of the Mg alloy chosen for this study is modeled after the high strength Mg-ZKQX6000 alloy (ZKQX6000, i.e. ZK60 with trace additions of Ag and Ca) discovered by Mendis et al. [2,3]. To efficiently explore the mechanical performance limits of the Mg-ZKQX6000 alloy, severe plastic deformation (SPD) processing via equal channel angular pressing (ECAP) was used herein. ECAP is well known [38,39] to produce exceptionally high mechanical strength via Hall-Petch [40,41] strengthening, i.e. grain refinement. The Mg-ZKQX6000 alloy was chosen both for its excellent mechanical properties [2] and the general consensus on the favorable biocompatibility of its constituent elements (i.e. Mg, Zn, Zr, Ag, and Ca) [12,14,15,42–44]. In this regard, Zn and Ca are essential nutritional elements [12,14], Zr has been reported to be biocompatible in vivo [12,15], and Ag is known for its antibacterial properties [42,43] and biocompatibility in vivo [44].

2. Materials and methods

Mg-ZKQX6000 (Mg 92.8 wt%, Zn 6 wt%, Zr 0.6 wt%, Ag 0.4 wt%, Ca 0.2 wt%) was formed via gravity die-casting. Alloying elements were melted at 750 °C under Ar in a boron nitride-coated steel crucible, stirred for 30 min, and cast into a steel mold. Once cooled to room temperature, edges of the billet were machined, and it was subsequently extruded in a 10 MN extruder. The billet and extrusion die were heated together to 300 °C prior to extruding at a profile velocity of 0.05 $m \cdot min^{-1}$. The processing imposed an extrusion ratio of 16 and yielded a final square cross-sectional area of 27.5 mm × 27.5 mm for the extruded billet. The extruded Mg-ZKQX6000 bar was cut into billets 150 mm long. These billets were annealed at 350 °C for 48 h under Ar and water quenched, yielding the initial “As Received” condition referred to as ‘ZKQX-AsRec’ throughout the text. Billets were machined to a 25 mm × 25 mm square cross-sectional area prior to ECAP through a 25.4 mm × 25.4 mm square channel.

In the present study, three billets of Mg-ZKQX6000 were ECAP processed by unique hybrid routes at low temperatures (200 °C to 125 °C). Throughout the text, these billets are referred to as ‘ZKQX-ECAP#1’, ‘ZKQX-ECAP#2’, and ‘ZKQX-ECAP#3’, following Table 1, which includes processing routes and temperatures for these billets. Here, route A imposes no rotation of the workpiece with respect to the

Table 1
Thermomechanical processing details and grain size measurements. Route A represents no rotation around the ED axis between passes, while route C represents a 180° rotation around the ED axis between passes (from Fig. 1). Grain sizes were measured from the RD_0 or FD planes.

Sample name	ECAP route & temperature	Average grain size (μm)
ZKQX-AsRec	None; As-received material	10.62 ± 7.18
ZKQX-ECAP#1	4C@200 °C + 180° rotation +2A@150 °C	0.92 ± 0.47
ZKQX-ECAP#2	2A@200 °C + 180° rotation +2A@150 °C + 1C@125 °C	0.54 ± 0.39
ZKQX-ECAP#3	4C@200 °C + 180° rotation +2A@150 °C + 1A@125 °C	0.51 ± 0.25

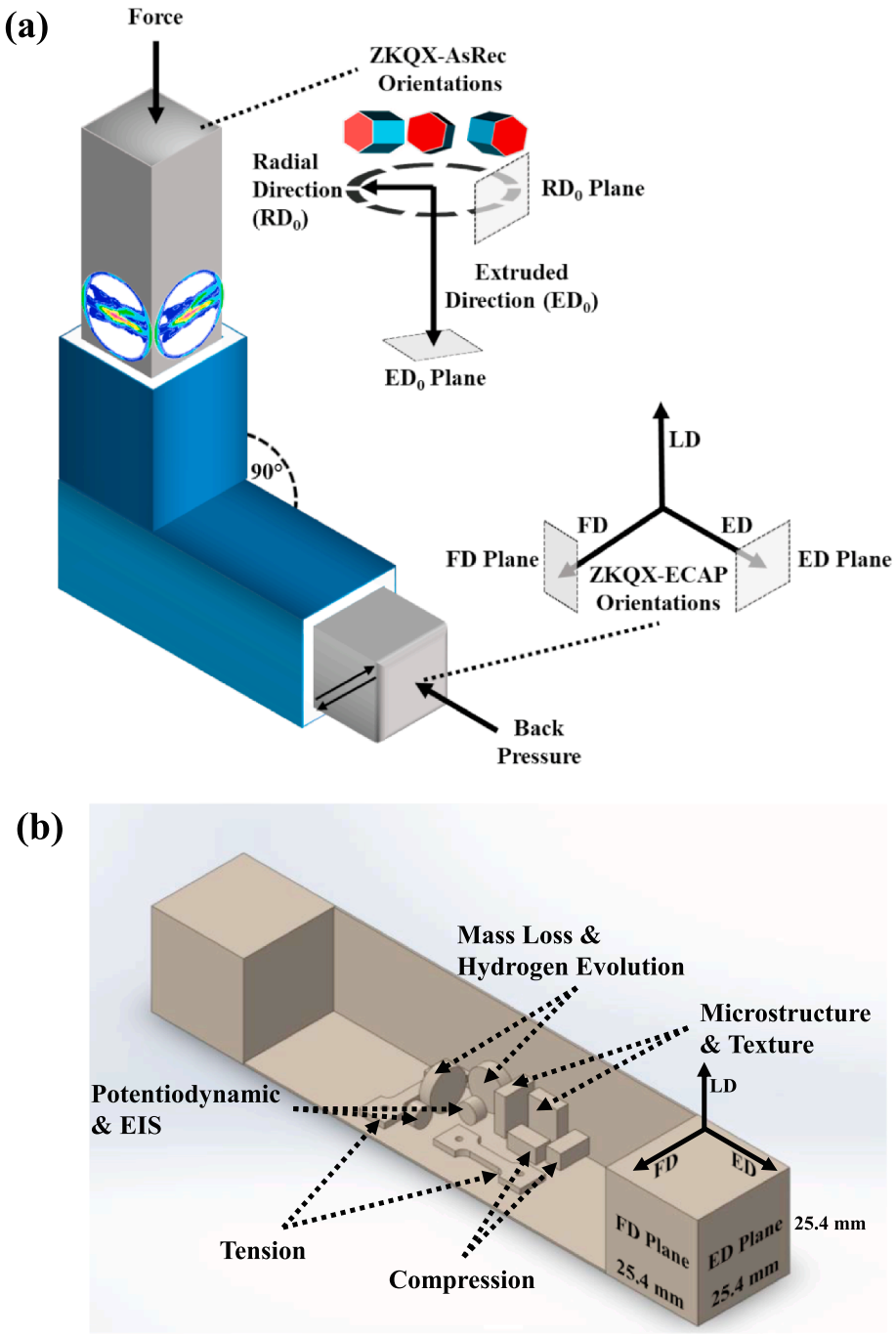

Fig. 1. (a) Schematic of the Mg-ZKQX6000 billets with respect to the ECAP press utilized in this study. Prior to ECAP, the basal pole figures showed that the (0002) basal planes lay parallel to the Extruded Direction (ED_0). Post ECAP orientations – FD: Flow Direction, ED: Extrusion Direction, LD: Longitudinal Direction. The sample planes exposed to the electrolyte during corrosion testing are shown with respect to the directions via the dashed gray rectangles. (b) Illustration of the different samples' locations with respect to the ECAP billets. Samples were cut from the center of the billet, away from the edges, as shown.

die, and route C imposes a 180° rotation about the long axis of the workpiece in between passes [45]. Billets were heated for 30 min to temperature prior to each ECAP pass. The Mg workpiece with its ZKQX-AsRec and ZKQX-ECAP#1–3 planes and directions with respect to the ECAP die is shown in Fig. 1a. ECAP was conducted using a die with a sharp, 90° corner. The ram speed of the ECAP press was 4.5 mm·min^{-1} at 200 °C and 150 °C, and 2.25 mm·min^{-1} at 125 °C. Back pressures of 20 MPa, 35 MPa, and 55 MPa were used for passes conducted at 200 °C, 150 °C, and 125 °C, respectively, to prevent shear localization-induced failure. Samples for experiments were cut via electrical discharge machining (EDM) from the mid-section of the ECAP billets to capture the most uniformly worked regions, as described by Barber et al. [45]. Fig. 1b captures the samples cut from the ECAP billets and their orientations.

To characterize the microstructure of the four conditions shown in Table 1, samples were cut along two planes for each (Fig. 1a–b) with the plane normal aligned along either the extruded direction (ED_0) or radial direction (RD_0) of ZKQX-AsRec, or along either the flow direction (FD) or extrusion direction (ED) of ZKQX-ECAP#1–3. To reveal grain boundaries, samples were polished via diamond paste to 0.1 μm and etched with acetic-picral (20 mL acetic acid, 3 g picric acid, 20 mL H_2O, 50 mL ethanol (95%)). Microstructures were imaged in an FEI Quanta-

600 scanning electron microscope (SEM), which allowed for scanning electron (SE) and backscattered electron (BSE) imaging. BSE images were conducted at an accelerating voltage of 15 KeV with a 3 mm spot size, from a working distance of approximately 10 mm. Grain sizes were measured from multiple SE images of the ZKQX-AsRec RD_0 and ZKQX-ECAP#1–3 FD planes with the ImageJ® software package. Energy dispersive X-ray spectrometry (EDS) quantified precipitate chemistries. Crystallographic texture was measured using a Bruker-AXS D8 X-ray diffractometer with Cu K_α (wavelength $\lambda = 0.15406$ nm) radiation.

Tension tests were conducted on flat, "dog-bone" tensile specimens with gauge sections 8 mm long and cross-sectional areas measuring 3 mm × 1.5 mm. Gauge sections were oriented along either the ED_0 or RD_0 for ZKQX-AsRec, or along either the ED or FD for ZKQX-ECAP#1–3 (see Fig. 1a–b). Compression testing was conducted on samples with gauge lengths of 8 mm and cross-sectional areas measuring 4 mm × 4 mm, likewise cut along the same sample orientations as the tensile samples (Fig. 1b). Tension and compression tests were performed with a strain rate of $5 \times 10^{-4}\ s^{-1}$ at room temperature, using an MTS test frame with an MTS extensometer to record strain values.

The potential between the precipitate and matrix was measured using scanning Kelvin probe force microscopy (SKPFM) in air at room temperature. SKPFM involves scanning the surface in the tapping mode to determine the topography on a line-by-line basis. This is followed by a rescan of the surface, where the tapping piezo is turned off, and AC voltage is applied to the tip, which stimulates oscillation of the cantilever in the presence of an electric field. In this manner, the potential difference between the precipitate and the matrix is measured.

All corrosion tests were performed in Hanks' balanced salt solution (HBSS) 1X® from VWR Life Sciences at 37 °C to mimic the conditions in the human body. HBSS is the most commonly used electrolyte for in vitro Mg corrosion testing [18]. Three techniques measured corrosion rates: 1) mass loss, 2) hydrogen gas collection, and 3) electrochemical calculations, which utilized experimentally derived potentiodynamic polarization (PDP) and electrochemical impedance spectroscopy (EIS) parameters. Samples for mass loss and hydrogen gas collection were 3 mm thick and exposed a circular cross-sectional area of 80 mm^2 for each plane of interest (Fig. 1b). The setup for mass loss and hydrogen gas collection is shown in Fig. 2, and consisted of the Mg-ZKQX6000 working electrode immersed in HBSS, placed beneath an inverted volumetric burette with a funnel attached to help collect evolved hydrogen gas bubbles. A physiological pH (7.4–7.6) of the HBSS was maintained throughout the 12 h of immersion by buffering the solution with a 0.1 M HEPES [4-(2-hydroxyethyl)-1-piperazineethanesulfonic acid] solution every 2 h [18]. The pH generally increased to about 8.5 after the first 2 h, but increased only to about 7.7 after the first buffer.

For mass loss and hydrogen evolution tests, samples were wrapped with carbon tape to expose only one plane to the electrolyte. Carbon tape did not produce any detrimental effects on corrosion of the Mg alloy samples. Epoxy could not be used for mass loss tests because it caused inaccuracies in mass measurements, producing effects such as mass *gain* in epoxy following testing. The mass loss, as measured gravimetrically with ± 0.1 mg resolution, was converted to corrosion current density (i_{corr}, in $A.cm^{-2}$) via Faraday's law [46]:

$$i_{corr}^{\Delta m} = znF = \frac{z\,\Delta m\,F}{a\,t\,A} \tag{3}$$

where z is the valence number of the Mg ion (2), n is the number of mols, F is Faraday's constant (96,485 $C.mol^{-1}$), Δm is the mass loss (g), a is the molar mass of Mg (24.305 $g.mol^{-1}$), t is time (12 h, or 43,200 s), and A is the surface area of the working electrode (80 mm^2). The volume of hydrogen gas released during immersion of the mass loss samples was measured based on a decrease in the solution volume in the glass burette. Here, i_{corr} ($A.cm^{-2}$) was calculated via a combination of the Ideal Gas Law and Faraday's Law [46]:

$$i_{corr}^{H2} = znF = \frac{z\,pVF}{RT} \tag{4}$$

where p is the pressure inside the burette (1 atm), V is the volume of hydrogen gas collected, R is the ideal gas constant, and T is temperature. Mass loss and hydrogen evolution tests were duplicated for each orientation to ensure repeatability.

Samples for electrochemical testing were placed within an epoxy mold, exposing only the plane of interest to HBSS (Fig. 1b). A shielded wire was connected to the sample to provide an electrical connection. The electrochemical testing program consisted of PDP and EIS performed on separate samples of a specified plane using a Gamry Reference 600 potentiostat. A classical three-electrode configuration was used in electrochemical experiments as follows: a 3 mm thick Mg-ZKQX6000 sample was the working electrode and exposed a circular cross-sectional area of 20 mm^2, a saturated calomel electrode (SCE) was the reference electrode, and a graphite wire was the counter electrode. Before starting PDP or EIS testing, the open circuit potential (OCP) measurement was performed for 60 min until the OCP reached a steady state condition. The PDP testing started from −0.3 V vs. OCP and finished at 0.5 V vs. OCP with a scan rate of 1 $mV.s^{-1}$. The EIS testing was performed every 2 h a total of six times for 12 h of total immersion time, which matched mass loss and hydrogen evolution immersion times. The EIS testing was performed from 10,000 Hz to 0.01 Hz with the sinusoidal potential of 10 mV after specimens reached a steady state condition. Following the first test, EIS tests were conducted after first buffering to a pH of 7.4 and then running 60 min at OCP. The i_{corr} ($A.cm^{-2}$) was calculated via a combination of EIS-estimated polarization resistance (R_p) and PDP-estimated Tafel constants [46]:

$$i_{corr}^{EIS} = \frac{\beta_a \beta_c}{2.303 R_p\,(\beta_a + \beta_c)} \tag{5}$$

where R_p is the polarization resistance ($\Omega.cm^2$), and β_a and β_c are anodic and cathodic Tafel constants, respectively (V). For accuracy and consistency across measurements, Tafel constants were derived from PDP results following guidelines from Kelly et al. [47], which stipulate (1) that anodic and cathodic branches of the polarization curve must exhibit a linear slope on a semilogarithmic scale, over at least one decade of current density, for a meaningful Tafel constant measurement, and (2) that the Tafel constant must be extrapolated from a point that is at a 50 to 100 mV offset from the E_{corr}. All samples for corrosion testing had a circular cross-sectional area to minimize the effects of geometric irregularities (e.g. corners) on altering surface energies and corrosive reactivity.

In-situ corrosion monitoring was conducted for the ZKQX-AsRec RD_0 plane and the ZKQX-ECAP#3 FD plane samples by wetting their surfaces with several drops of HBSS and monitoring this region with an optical microscope equipped with a video recorder. These tests, called "drop tests", lasted to up to an hour, so the solution was refreshed every 10 min. The in-situ corrosion monitoring allowed for micro-galvanic effects to be observed directly in real time.

3. Results and discussion

3.1. Microstructure and mechanical properties

SE (Fig. 3) and BSE (Figs. 4–5) show microstructures of ZKQX-AsRec and ZKQX-ECAP#1–3. Fig. 3a–d shows grains for ZKQX-AsRec and ZKQX-ECAP#1–3, with the corresponding lognormal grain size distributions (Fig. 3e) and crystallographic textures capturing $(10\bar{1}0)$ prismatic and (0002) basal plane orientations. In Fig. 3, average grain diameters μ with their standard deviations σ are shown for each. Fig. 3a–d shows that white precipitates (e.g. red arrows) were refined via ECAP, and they often heavily obscured grain boundaries (e.g. Fig. 3b). Furthermore, perhaps because the ECAP routes selected for ZKQX-ECAP#1–3 were unique hybrid routes designed for optimal

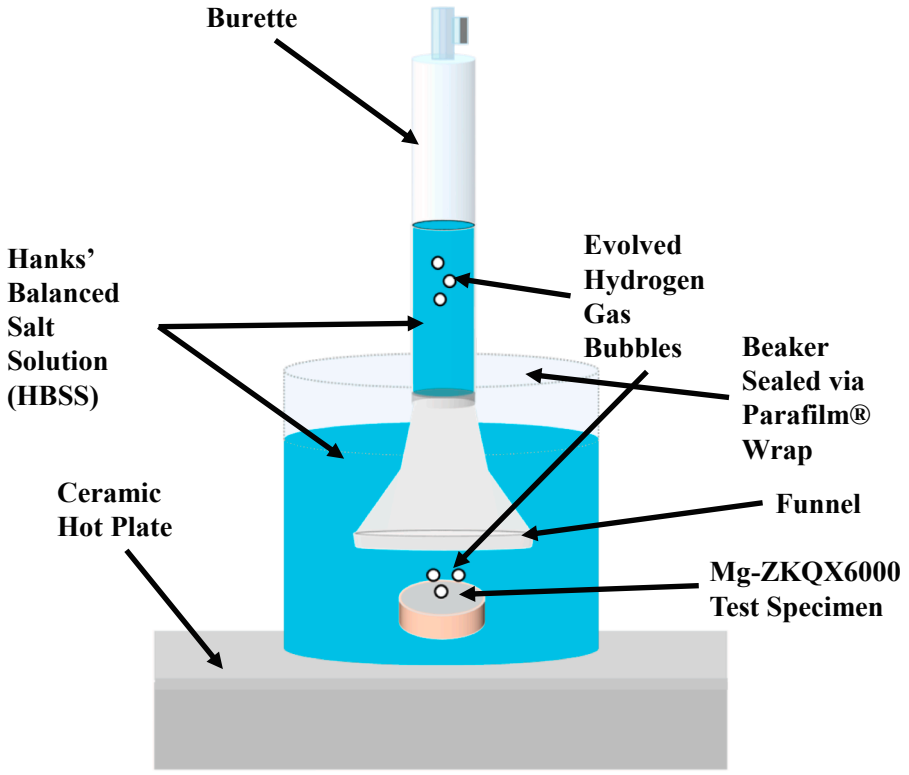

Fig. 2. Experimental test setup for the mass loss and hydrogen gas collection, conducted in Hank's Balanced Salt Solution (HBSS) at 37 °C at a pH of 7.4 for 12 h. The burette was used to measure the volume of evolved hydrogen gas.

strengthening in Mg-ZK60 [48], the grain size via ECAP showed some heterogeneity, as larger grains (e.g. blue arrows) could sometimes be found. Fig. 3e shows, overall, that ZKQX-AsRec exhibits the largest heterogeneity in grain size, a combined result of its larger average grain size versus ZKQX-ECAP#1–3 and its subjection to extrusion, which produced elongated stringer grains (e.g. blue arrows in Fig. 3a) oriented parallel to the ED_0. Regarding heterogeneity, it is worth mentioning that large, unsheared grain and precipitate clusters on the order of tens of microns were found sporadically in all ECAP cases, whose sizes are not precisely reflected in the grain size distributions due to their random occurrence and their abnormal morphology. Note that large stringer grains in ZKQX-AsRec (e.g. blue arrow in Fig. 3a) were also found sporadically and were likewise difficult to quantify due to their very large aspect ratios.

Overall, ZKQX-ECAP#1–3 have an average grain size an order of magnitude smaller than ZKQX-AsRec. Following the ECAP routes shown in Table 1, the finest grain sizes of about 500 nm were produced at the lowest processing temperature, 125 °C (Fig. 3b–d). Crystallographic textures demonstrate that ECAP generally softened the strong extrusion texture of ZKQX-AsRec, with the exception of ZKQX-ECAP#3, which has a pretty similar texture. While the (0002) pole figure for ZKQX-AsRec demonstrates a typical extrusion texture, with the c-axes aligning normal to the ED_0, ZKQX-ECAP#2 has most *c*-axes aligned along the LD, and ZKQX-ECAP#1 shows an intermediate texture with *c*-axes aligned along primarily the LD but also along the FD.

Due to the large amount of precipitates found in the SE images (Fig. 3a–d), Fig. 4 (low magnification, 90×) and Fig. 5 (high magnification, 2000×) are included to study the effect of ECAP on precipitate morphology, distribution, and size. Figs. 4–5 are BSE images captured at high contrast to clearly show precipitates (in white) against the Mg matrix (in black). In Fig. 4a, low magnification BSE images are taken from the RD_0 or FD planes, where precipitates (in white) were initially oriented along the ED_0 for ZKQX-AsRec. However, ECAP broke down these large precipitates and made them less elongated along the ED. BSE images in Fig. 4b taken from the ED_0 or ED planes show that precipitate distributions were less elongated and more equiaxed in comparison to the RD_0 and FD planes of Fig. 4a. While it may appear from Fig. 4a that ZKQX-ECAP conditions show a lower volume fraction of precipitates, in Fig. 5a–d higher magnification images of these precipitate regions clearly show that ECAP processing broke down the large precipitates into finer precipitates. A similar finding was observed for the ED planes, but is not shown here for brevity's sake. As shown in Fig. 5, precipitates for all conditions were Zn-Zr enriched according to EDS measurements. Apparently, for ZKQX-AsRec, the imposed 48 h of heat treatment was unsuccessful in moving such precipitates into solid solution, indicating that Zn-Zr can form insoluble intermetallic compounds in Mg alloys.

The uniaxial tension and compression responses are shown in Fig. 6, whose mechanical properties are summarized in Table 2. Fig. 6a shows responses along the ED_0 and ED, and Fig. 6b shows them along the RD_0 and FD. From Fig. 6b, the best yield strengths occurred along the FD at about 360 MPa for both ZKQX-ECAP#2 and ZKQX-ECAP#3. Here, an ultra-fine grain size of 0.54 ± 0.39 μm and 0.51 ± 0.25 μm, respectively, had been measured; in contrast, ZKQX-ECAP#1, with a grain size of 0.92 ± 0.47 μm, had a tensile yield strength of about 340 MPa along the FD. In Fig. 6b, ultra-high ultimate tensile strengths (UTSs) of about 400 MPa along the FD were obtained for ZKQX-ECAP#2 and ZKQX-ECAP#3, followed closely by ZKQX-ECAP#1 at about 350 MPa. After ECAP, ultimate compressive strengths (UCSs) were, with the exception of ZKQX-ECAP#2 along the ED, quite high (> 500 MPa, which is exceptional for Mg alloys [24]). In addition, ZKQX-ECAP#1–3 consistently had significantly higher yield strengths than ZKQX-AsRec under tension and compression, reflecting Hall-Petch [40,41] strengthening. A reduction in tension-compression asymmetry is also evident from both Fig. 6a–b and Table 2. Given the nature of orthopedic implants as supportive devices bearing compressive loads, the compression responses may be more relevant than the tensile responses for the applications in mind.

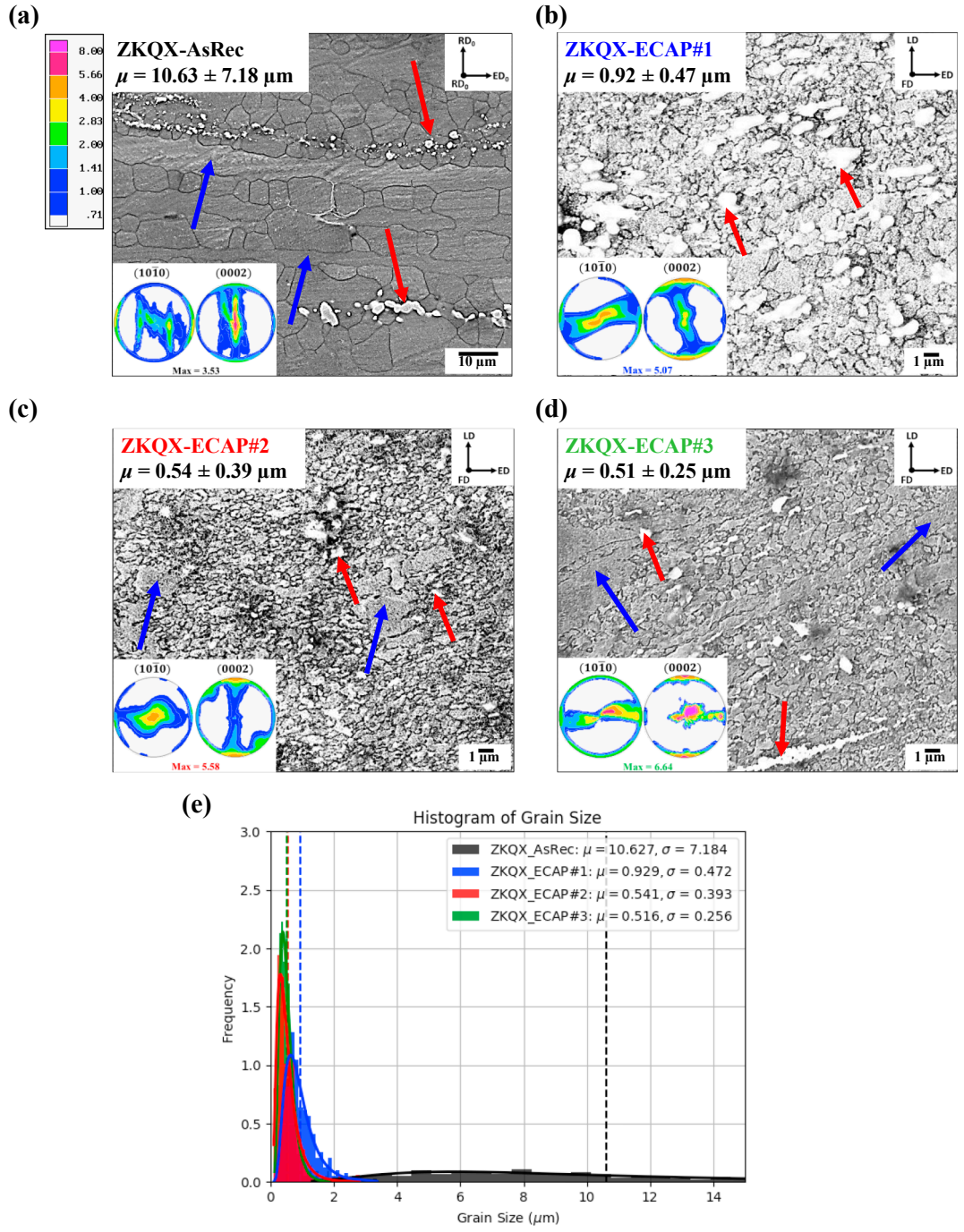

Fig. 3. Scanning electron (SE) images and crystallographic texture pole figures capturing the $(10\bar{1}0)$ prismatic and (0002) basal planes of (a) ZKQX-AsRec RD_0 plane, (b) ZKQX-ECAP#1 FD plane, (c) ZKQX-ECAP#2 FD plane, and (d) ZKQX-ECAP#3 FD plane. The texture plot scale for all cases is shown in (a). Red arrows show Zn-Zr enriched precipitates, and blue arrows show larger grains indicative of microstructural heterogeneity. (e) shows the corresponding grain size distributions and average grain diameters μ (marked with dashed lines) with their standard deviations σ. (For interpretation of the references to colour in this figure legend, the reader is referred to the web version of this article.)

Unfortunately, Fig. 6 and Table 2 show that ECAP resulted in poor elongation to failure (ε_f) levels in tension and compression. As explained below, the low ε_f, which is often below 10% after ECAP, is likely derived from precipitate embrittlement effects caused by the breakdown of large precipitates during ECAP, as was shown in Figs. 4–5. Generally in Mg, grain refinement has been reported to actually improve ductility by suppressing twinning modes [34,49], which are known to cause strain hardening and localization, leading to void nucleation and growth which, in turn, leads to mechanical failure [9,50–52]. At a sufficiently refined grain size, twinning modes can possess higher CRSS values than prismatic or pyramidal slip systems, leading to suppressed twinning activity and producing higher ductility [23]. Razavi et al. [8], for instance, took advantage of this effect for Mg-AZ31 by using ECAP to achieve a UTS of 455 MPa with a respectable ε_f of 12.7% along the FD.

As grain sizes and crystallographic textures are comparable, the most obvious difference between the work conducted by Razavi et al. [8] and the present study is the different alloys chosen for each. In their work [8], AZ31, which has only about 4.5 wt% of alloying elements, was solution heat treated more effectively prior to ECAP than in the

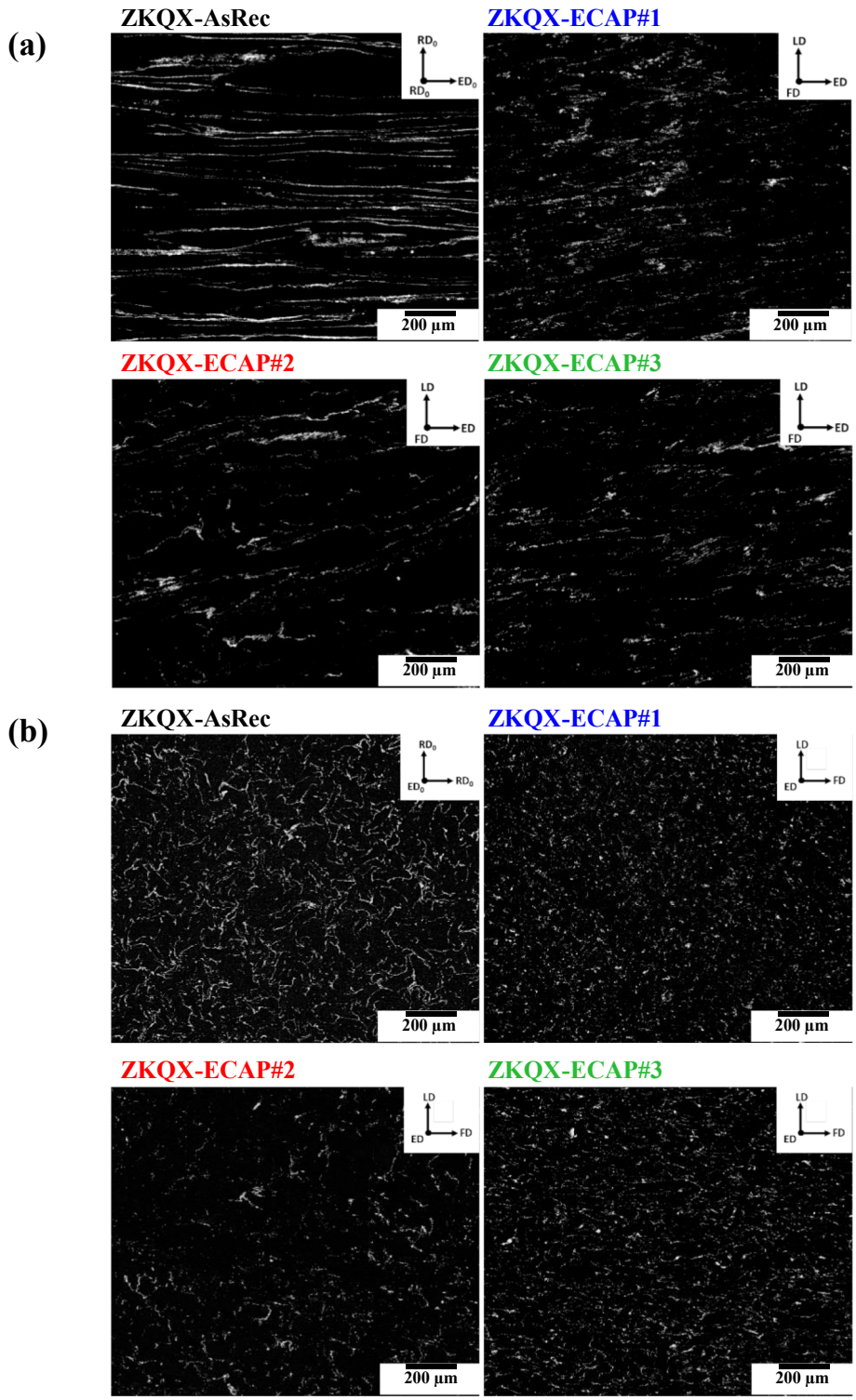

Fig. 4. Low magnification (90×), high-contrast backscattered electron (BSE) images capturing precipitate distributions in white for (a) the ZKQX-AsRec RD_0 plane and ZKQX-ECAP#1–3 FD planes, and (b) the ZKQX-AsRec ED_0 plane and ZKQX-ECAP#1–3 ED planes. ECAP in both the ED and FD planes altered the sizes, alignments, and distributions of the precipitates in comparison to ZKQX-AsRec.

present work. The ZKQX6000 alloy used herein has about 7 wt% of alloying elements, and the large Zn-Zr enriched particles (Fig. 5a) proved very difficult to dissolve into the matrix despite a 48-hour solution heat treatment at 350 °C, where Zn has the maximum solid solubility in Mg. It was expected herein that the combined effects of texture weakening and grain refinement from ECAP would minimize twinning activity while favoring activation of harder slip modes [8,23], producing improved strength and ductility. Thus, the low ductility observed can be attributed to the precipitate-induced embrittlement rather than texture effects or twinning-induced failure.

As discussed in Ref. [53], support for precipitate embrittlement is apparent when the precipitate images of Fig. 4 are compared with the experiments of Fig. 6. In particular, according to Fig. 4a for ZKQX-AsRec, ε_f is only about 7% when the tensile axis is along the RD_0, i.e. normal to

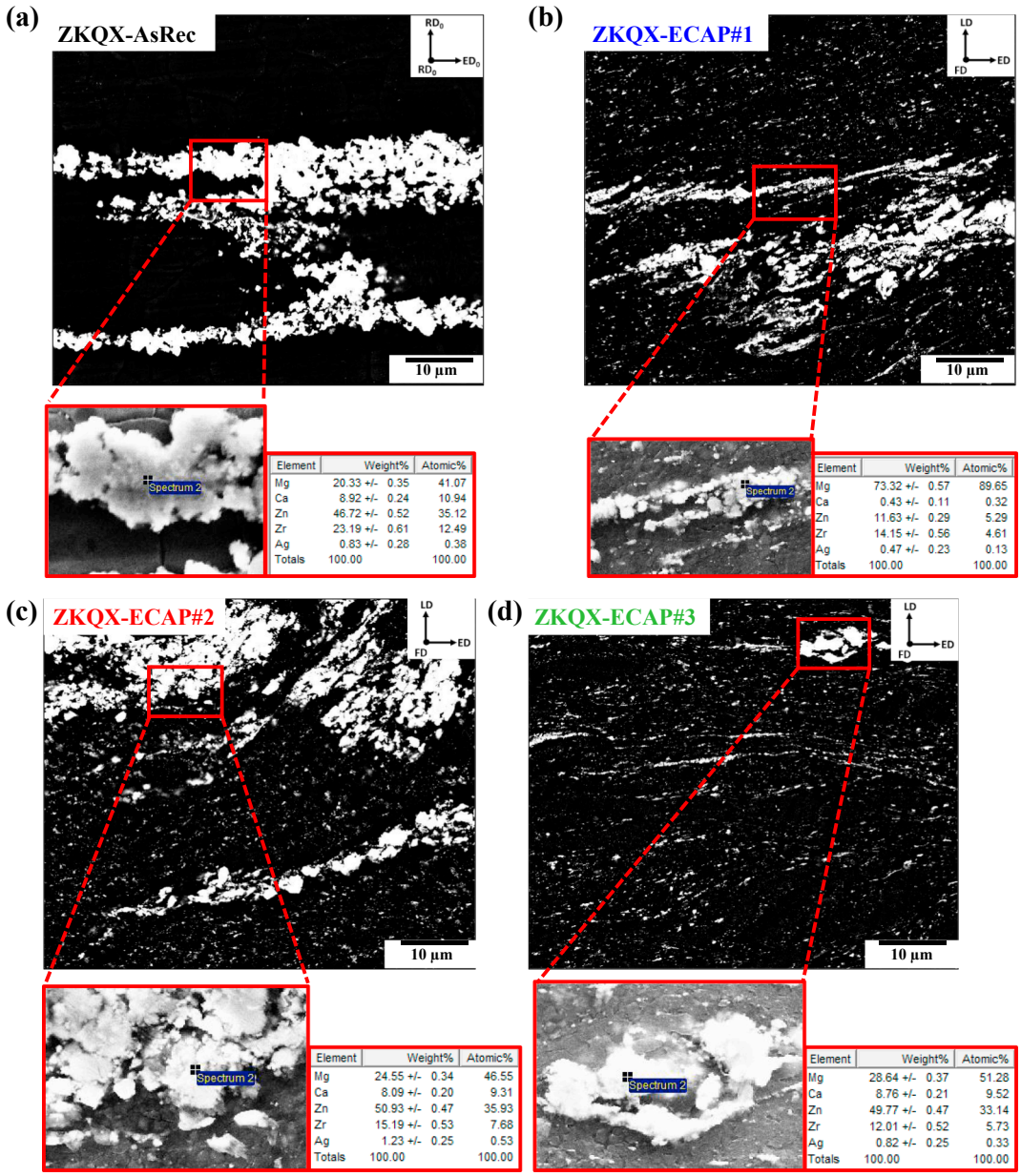

Fig. 5. High magnification (2000×), high contrast BSE images showing the Zn-Zr enriched precipitates in white, along with their energy dispersive X-ray spectroscopy (EDS) chemistries. (a) shows the ZKQX-AsRec RD_0 plane, (b) shows the ZKQX-ECAP#1 FD plane, (c) shows the ZKQX-ECAP#2 FD plane, and (d) shows the ZKQX-ECAP#3 FD plane. For each, "Spectrum 2" marks the exact locations where precipitate chemistries were measured via EDS. ECAP clearly has broken down and redistributed the large precipitates as finer precipitates in the matrix.

precipitates elongated along the ED_0. In contrast, ε_f under compression along the same axis is a respectable 14%. As shown in Ref. [53], the interface between precipitates and the Mg matrix delaminates during tension along the RD_0, proving that precipitate embrittlement occurs for this material. The effects of precipitate orientation are therefore important, yet are nearly impossible to follow for ZKQX-ECAP#1–3, as the distribution, morphology, and sizes of precipitates have been significantly altered through each ECAP pass and are not trackable. To avoid poor ε_f after ECAP, the authors suggest utilizing low (< 4 wt%) amounts of alloying elements in Mg alloys, where all alloying additions should be capable of being fully dissolved into the solid solution prior to ECAP.

3.2. Corrosion rates

As shown in Section 3.1, ECAP enhanced mechanical strength to ultra-high strength levels for several conditions of the ZKQX6000 alloy by creating an ultra-fine grain size via superplastic deformation at low temperatures. While ECAP refined grain size, it also refined precipitates and modified their morphologies and distributions in ZKQX-ECAP#1–3, as seen in Figs. 3–5. In the interest of utilizing this alloy for biomedical implants, the effects of microstructural changes on corrosion rates are investigated in this section.

In this regard, PDP scans were first conducted for all conditions and are shown in Fig. 7. Here, all corrosion potentials (E_{corr}) hovered around −1.5 V vs. SCE, which is typical for Mg alloys. From Table 4, the Tafel constants (β_c and β_a) were nearly identical for all conditions. In this regard, a β_c of about 0.25 $V.dec^{-1}$ and a β_a of about 0.05 $V.dec^{-1}$ are in the expected ranges, as lower values of β_a (i.e. below 0.15 $V.dec^{-1}$) occur because Mg is nonpolarizable, and higher values of β_c (i.e. between 0.20 and 0.30 $V.dec^{-1}$) are normal [46]. In Fig. 7, there was no indication of a passive window, suggesting that all samples are spontaneously active in HBSS. A clear trend in corrosion

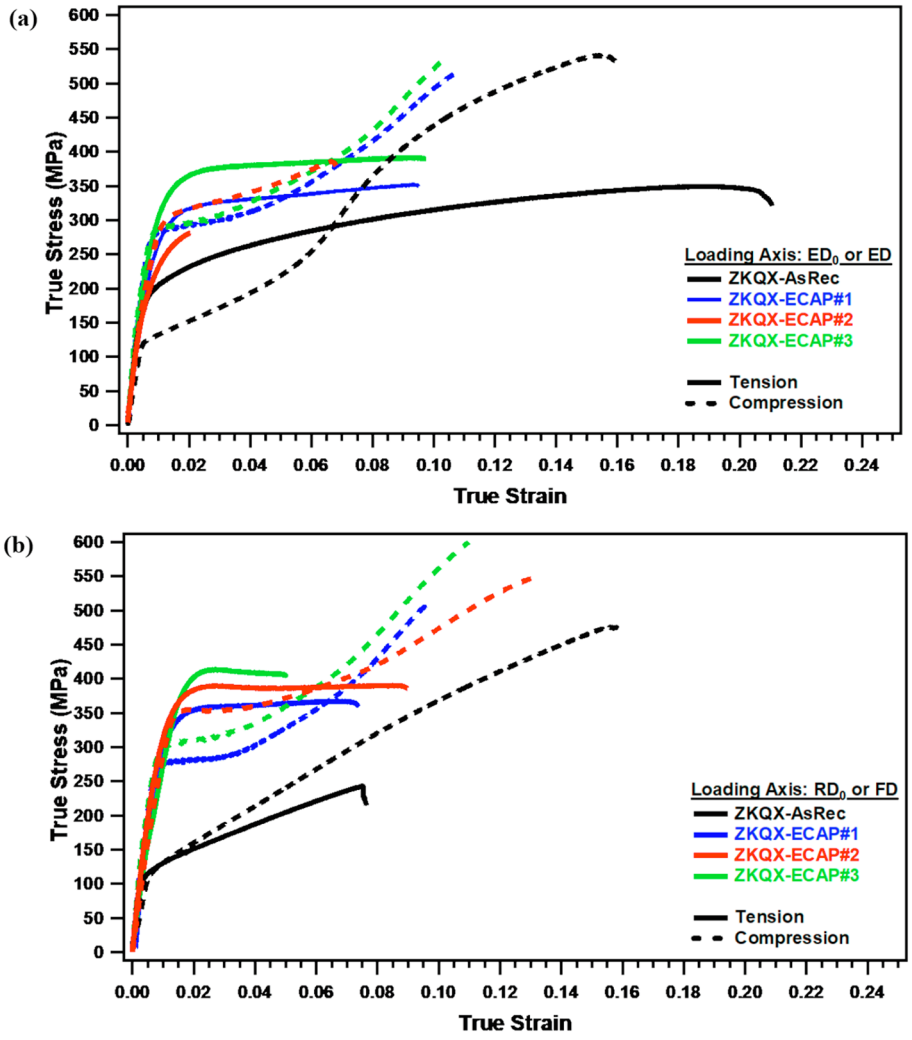

Fig. 6. True stress vs. true strain curves for all conditions tested under uniaxial tension and compression. (a) shows the flow curves tested along the ED_0 (ZKQX-AsRec) and ED (ZKQX-ECAP#1–3), while (b) shows them along the RD_0 (ZKQX-AsRec) and FD (ZKQX-ECAP#1–3). Table 1 reports the ECAP conditions and resultant grain sizes, while Table 2 summarizes the mechanical properties.

rate was not obvious from the PDP results, as all exhibited similar E_{corr} and Tafel constants. However, there is substantial evidence [18,19,35,46,54] that PDP testing cannot be used directly for Mg to determine accurate corrosion rates. For instance, Shi et al. [54] reported a large deviation in corrosion rates determined from Tafel extrapolation when compared with corrosion rates derived from mass loss and evolved hydrogen gas collection. Song et al. [19] also carried out PDP studies that produced similar corrosion rate estimates for

Table 2
Tabulated mechanical properties for the Mg-ZKQX6000 alloy from uniaxial tension and compression tests. Values here are true stress and strain, extracted from the flow curves shown in Fig. 6; RD_0 and ED_0 pertain solely to ZKQX-AsRec.

Sample	Tension along the ED_0 or ED				Tension along the RD_0 or FD			
	σ_y (MPa)	σ_{UTS} (MPa)	ε_u (%)	ε_f (%)	σ_y (MPa)	σ_{UTS} (MPa)	ε_u (%)	ε_f (%)
ZKQX-AsRec	198	345	17.5	19.8	120	242	6.7	6.8
ZKQX-ECAP#1	295	351	8.3	8.3	339	365	5.7	6.1
ZKQX-ECAP#2	232	279	1	1	361	390	1.5	7.6
ZKQX-ECAP#3	338	389	8.3	8.3	359	412	1.4	3.6

Sample	Compression along the ED_0 or ED				Compression along the RD_0 or FD			
	σ_y (MPa)	σ_{UCS} (MPa)	ε_u (%)	ε_f (%)	σ_y (MPa)	σ_{UCS} (MPa)	ε_u (%)	ε_f (%)
ZKQX-AsRec	119	538	–	13.9	112	473	–	14.5
ZKQX-ECAP#1	289	510	–	8.8	273	502	–	7.8
ZKQX-ECAP#2	301	382	–	5.3	349	540	–	11.3
ZKQX-ECAP#3	290	520	–	8.2	305	595	–	8.8

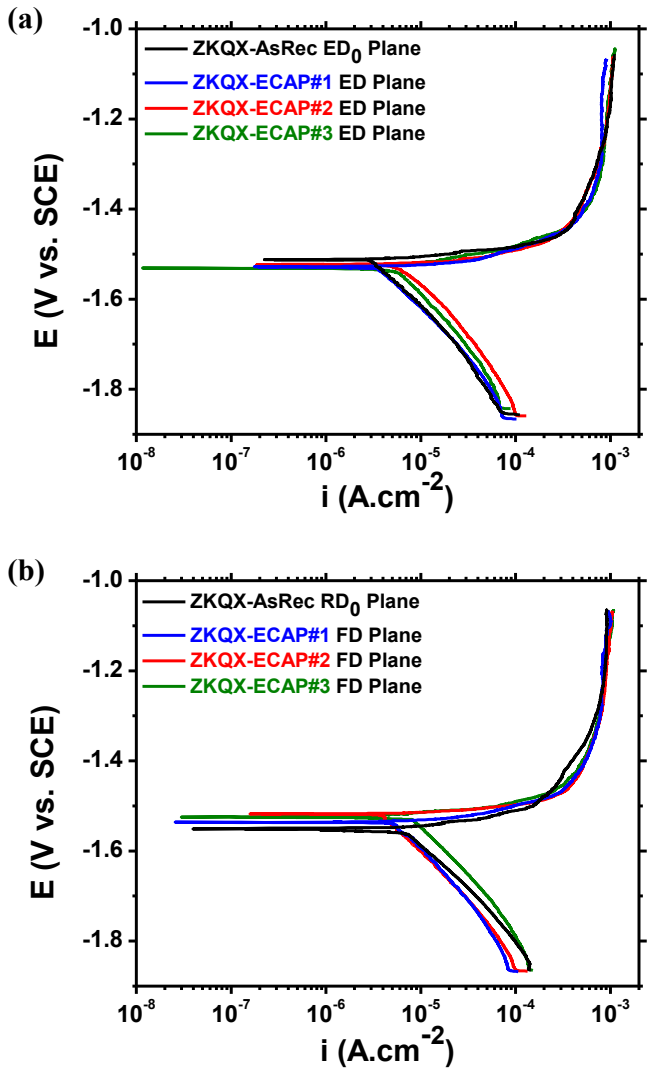

Fig. 7. Potentiodynamic polarization (PDP) plots for (a) ZKQX-AsRec ED_0 vs. ZKQX-ECAP#1–3 ED planes and (b) ZKQX-AsRec RD_0 vs. ZKQX-ECAP#1–3 FD planes. Corrosion rates calculated via Tafel extrapolation were unreliable and resulted in poor accuracy in comparison with the other testing methods. Thus, Tafel constants from these plots (shown in Table 4) were used to calculate more accurate corrosion rates via an alternate method (Eq. (5)).

different Mg alloys with varying microstructures and very different mass loss corrosion rates. Because a single anodic and cathodic reaction are prerequisites for Tafel extrapolation to provide an acceptable estimate of corrosion rate [27], Song et al. [19] argued that misleading Tafel extrapolation estimates of corrosion rate are due to the fact that magnesium corrosion violates fundamental Tafel requirements. In particular, the negative difference effect in Mg produces hydrogen during anodic polarization, where the hydrogen gas is increasingly liberated with higher anodic overpotentials, resulting in misleading corrosion rates from PDP scans. With this in mind, in the present study corrosion rates were derived by combining electrochemical techniques of Tafel extrapolation with EIS-estimated R_p values, according to Eq. (5), which is based on the study by King et al. [46]. There, Tafel extrapolation and EIS were combined, and similar corrosion rate values from electrochemical techniques, mass loss, and hydrogen gas collection tests were obtained [46].

EIS results in the form of Nyquist plots are shown in Fig. 8a–b for hours 10 to 12 of immersion, and Fig. 8c captures the plot legends. Here, experimental results were simulated via the software package ZView® according to the electrochemical equivalent circuit (EEC) design shown in Fig. 8d, whose parameters are captured in Table 3. The EEC of Fig. 8d was modeled after Ref. [46] to include the minimum number (2) of capacitive elements with an inductive element to accurately simulate the EIS raw spectra of Fig. 8a–b. According to the EEC model of Fig. 8d, when corrosion occurred, the $MgO/Mg(OH)_2$ film was formed, and there was a consequent charge separation at the Mg alloy substrate and $MgO/Mg(OH)_2$ film interface. This effect is represented by a double layer capacitance ($CPE_{double\ layer}$) and a resistance (R_t) of the charge transfer reaction (Eq. (1)) at this interface in Fig. 8d. Also, separation of charge by the $MgO/Mg(OH)_2$ film between the substrate and solution is represented as film capacitance (CPE_{film}), with a corresponding resistance (R_{film}). During the fitting, a constant phase element (CPE) was utilized instead of capacitance to represent surface heterogeneities, deviation from capacitance behavior, and the dispersion effect. Calculated CPE exponents (α) were considerably below 1 (Table 3), and thus much lower than ideal capacitive behavior (i.e. when $\alpha = 1$). In the EEC (Fig. 8d), the adsorption process occurring during corrosion is represented by inductance ($L_{adsorption}$), which is in series with the resistance of this adsorption process ($R_{adsorption}$). Finally, $R_{solution}$ is the resistance of the solution (HBSS).

The resulting EEC simulation fits from the model described above are shown via solid lines in the Nyquist plots in Fig. 8a–b and generally superimposed well onto the experimental data. Here, it is evident that the most difficult experimental spectra to simulate were for ZKQX-AsRec at low frequencies, which is probably related to a relatively accelerated adsorption of intermediate species. Recall that the inductive loop at low frequencies is usually associated with the adsorption of intermediate species on the metal surface. Given the aqueous solution, the adsorbed species on the Mg electrode are likely $Mg(OH)_2$ [4], which is unstable at physiological pH levels [18]. From the EEC, R_p is calculated for each condition via [46]:

$$\frac{1}{R_p} = \frac{1}{R_{film} + R_t} + \frac{1}{R_{adsorption}}, \tag{6}$$

by which the R_p of all samples, and subsequently the corrosion current density according to Eq. (5), were calculated. As marked (blue stars) for ZKQX-AsRec in Fig. 8a, R_p is defined as the impedance Z' at a frequency of 0, while the charge transfer resistance R_t is defined as the impedance Z' at an intermediate frequency (i.e. between 0 and infinity) [46]. As all Nyquist experimental spectra exhibit an inductive loop (Fig. 8a–b), R_p rather than R_t was used for corrosion rate calculations for better accuracy [46]. The Nyquist plots of Fig. 8a (ED_0 or ED planes) and Fig. 8b (RD_0 or FD planes) show the capacitive loops at the negative imaginary impedance ($Z'' < 0$) and inductive loops at the positive imaginary impedance ($Z'' > 0$). Overall, the differences in impedance of capacitive and inductive loops between the two plots are small, indicating similar kinetics. Fig. 8a–b Nyquist plots showed that ECAP increased corrosion rate across all conditions, as indicated (according to Eq. (5)) by a decrease in R_p for ZKQX-ECAP#1–3 in comparison to ZKQX-AsRec. Corrosion rates were calculated as corrosion current densities (i_{corr}) following Eq. (5) and are tabulated in Table 4.

In Table 4 and Fig. 9, i_{corr} derived from mass loss, evolved hydrogen gas, and electrochemical testing are tabulated and compared. From Fig. 9, the electrochemical corrosion rates (gray) generally agree across all samples with mass loss (orange) and hydrogen evolution (blue) corrosion rates. These results support the methodology proposed by King et al. [46] for deriving consistent corrosion rates across multiple testing methods in Mg alloys. In addition, they indicate that, despite the poor simulation fit of ZKQX-AsRec (Fig. 8a–b) at low frequencies, the R_p values thereby derived are reasonably accurate.

The main finding of Fig. 9 is that ECAP processing dramatically increased corrosion rates. Although comparisons are somewhat difficult due to the wide variety of different testing procedures and conditions, overall ZKQX-AsRec in a buffered HBSS solution already exhibits a fairly rapid corrosion rate compared to other Mg alloys [16,18], and this rate only accelerates due to ECAP. The high corrosion current

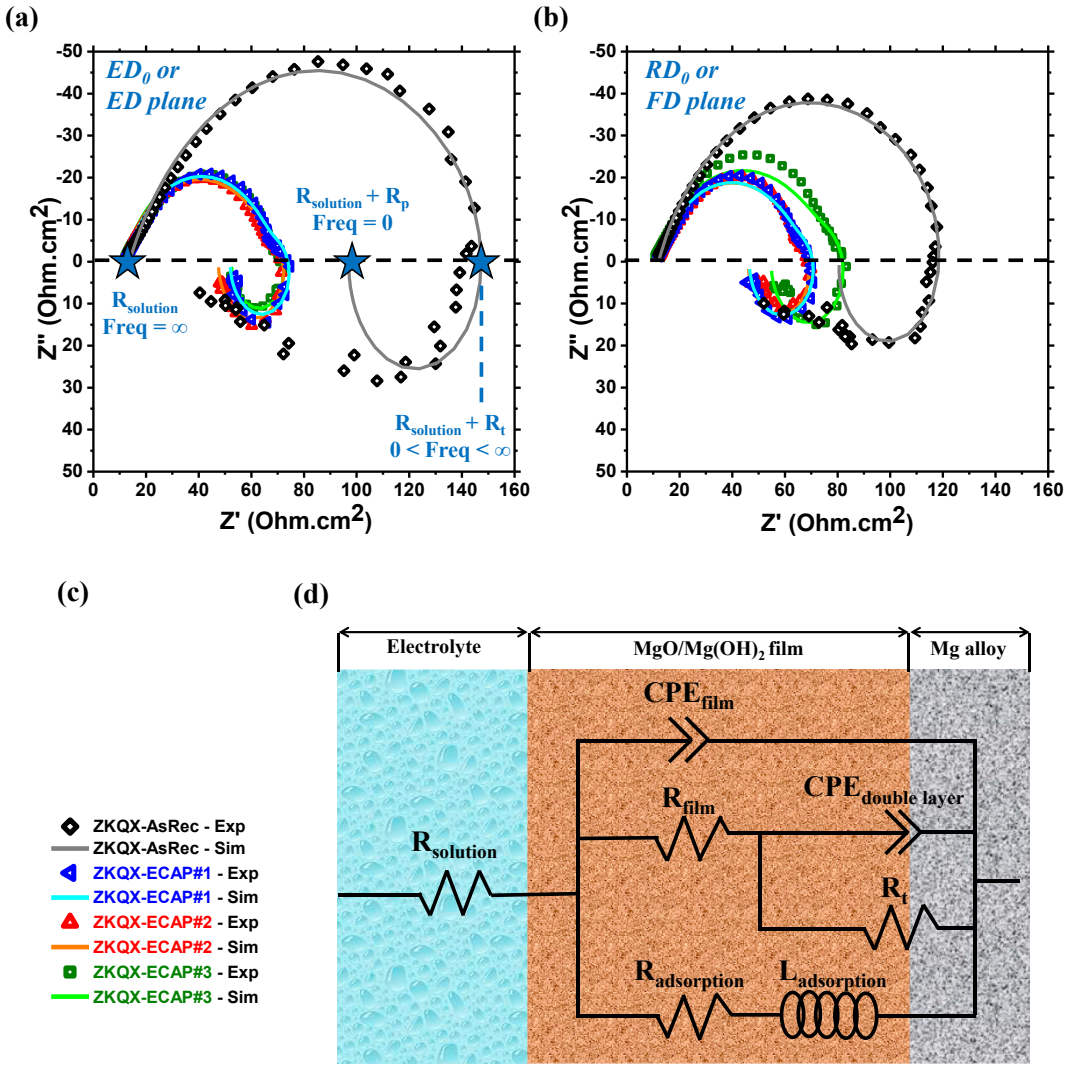

Fig. 8. Electrochemical impedance spectroscopy (EIS) results. (a) shows Nyquist plots for the ED_0 or ED planes. (b) shows the Nyquist plots for the RD_0 or FD planes. (c) captures the legends for (a, b). (d) shows the electrochemical equivalent circuit (EEC) which was used to simulate the experimental spectra of (a, b). EEC parameters are listed in Table 3. In (a), an example of $R_{solution}$, R_t, and R_p impedances are shown via blue stars for ZKQX-AsRec ED_0 plane. Overall, (a, b) demonstrate that ZKQX-ECAP#1–3 corroded faster (with a smaller R_p) than ZKQX-AsRec. (For interpretation of the references to colour in this figure legend, the reader is referred to the web version of this article.)

Table 3
Parameters captured via electrochemical impedance spectroscopy (EIS) measurements for the Mg-ZKQX6000 alloy during hours 10–12 of immersion in HBSS. The corresponding equivalent circuit can be found in Fig. 8d.

Sample	$R_{solution}$ $\Omega{\cdot}cm^2$	CPE_{film} $\mu F{\cdot}s^{n-1}{\cdot}cm^{-2}$	α_{film}	R_{film} $\Omega{\cdot}cm^2$	$CPE_{double\ layer}$ $\mu F{\cdot}s^{n-1}{\cdot}cm^{-2}$	$\alpha_{double\ layer}$	R_t $\Omega{\cdot}cm^2$	L $\Omega{\cdot}s{\cdot}cm^2$	$R_{adsorption}$ $\Omega{\cdot}cm^2$	R_p $\Omega{\cdot}cm^2$
ZKQX-AsRec ED_0 Plane	13.74	173.67	0.71	139.93	20,254.78	0.71	23.55	121.48	198.21	89.59
ZKQX-ECAP#1 ED plane	12.95	260.73	0.79	55.01	21,783.44	0.90	25.51	74.58	74.65	38.74
ZKQX-ECAP#2 ED plane	12.17	362.64	0.77	55.09	23,312.10	0.91	14.91	97.73	69.98	35.00
ZKQX-ECAP#3 ED plane	11.97	398.30	0.79	53.77	25,350.32	0.94	13.47	128.94	71.50	34.65
ZKQX-AsRec RD_0 Plane	11.58	220.36	0.75	111.47	23,108.28	0.62	17.66	110.10	147.19	68.79
ZKQX-ECAP#1 FD plane	12.17	343.03	0.76	55.15	25,542.93	0.91	7.85	138.36	75.36	34.31
ZKQX-ECAP#2 FD plane	12.36	383.64	0.74	55.34	26,496.82	0.91	9.81	132.47	69.28	33.58
ZKQX-ECAP#3 FD plane	10.79	373.45	0.74	66.14	23,587.26	0.91	13.74	193.11	98.13	44.03

densities reported in Fig. 9 result partially from buffering of the electrolyte to bodily pH levels (7.4), which prevents the formation of a stable, protective $Mg(OH)_2$ film that begins forming at a pH of 9 and reaches full passivation at a pH of 12 [4,18]. In addition, ECAP changes grain size, crystallographic texture, and precipitate features (Figs. 3–5), suggesting that their modifications affected corrosion rate. With this in mind, the effects of the microstructural features on corrosion are investigated in the next section.

3.3. Microstructural effects on corrosion rates

Perhaps the most obvious effect of ECAP in the present study was strengthening via grain refinement. While grain refinement is typically associated with a reduced corrosion rate [5,7,11,28–31,55] for both

Table 4
Typically measured mass loss (Δm), volume of evolved hydrogen gas (ΔV_{H2}), and Tafel constants (β_c, β_a) for each condition. Such values were used according to Eqs. (3)–(5) as appropriate to calculate the mass loss, evolved hydrogen gas, or electrochemical (EIS) corrosion current densities (i_{corr}) shown.

Sample	Δm mg	ΔV_{H2} mL	β_c V·dec^{-1}	β_a V·dec^{-1}	I_{corr} Δm μA·cm^{-2}	I_{corr} ΔV_{H2} μA·cm^{-2}	I_{corr} EIS μA·cm^{-2}
ZKQX-AsRec ED_0 Plane	0.9	0.95	0.25	0.05	210.71	211.82	201.95
ZKQX-ECAP#1 ED plane	1.9	2.0	0.25	0.05	444.83	445.94	467.04
ZKQX-ECAP#2 ED plane	2.1	2.2	0.25	0.05	491.65	490.53	516.99
ZKQX-ECAP#3 ED plane	2.3	2.5	0.25	0.05	538.48	557.42	522.11
ZKQX-AsRec RD_0 Plane	1.1	1.2	0.23	0.04	257.53	267.56	215.10
ZKQX-ECAP#1 FD plane	2.3	2.3	0.25	0.05	538.48	512.83	527.28
ZKQX-ECAP#2 FD plane	2.4	2.5	0.25	0.05	561.89	557.42	538.84
ZKQX-ECAP#3 FD plane	1.8	2	0.25	0.05	421.42	445.94	410.89

pure Mg and Mg alloys, many studies [25,32–35] have reported the opposite effect. The mechanism for improving corrosion resistance with grain refinement has been attributed to the corresponding higher inclination for passive oxide film formation [56]. Aung and Zhou [31] also explained that grain boundaries provide a corrosion barrier in the AZ31B Mg alloy, which was supported by an increase in the corrosion rate when there was grain growth. However, these arguments seem to violate the basic knowledge of a grain boundary as an active site in the metal; in general, a grain boundary is a defect in the form of an atomic mismatch, seemingly a wall of dislocations, between grains. Since dislocations are considered to be more susceptible to corrosion attack [25,31,32], there is no obvious reason for a grain boundary to halt the corrosion process. Indeed, Song et al. [57] demonstrated that corrosion in AZ31 does not stop at grain boundaries; instead, it preferentially occurs along grain boundaries. Such conflicting findings suggest that the effect of grain size alone is difficult to determine, especially in multicomponent alloys. In the current study, it is evident that the effect of grain size refinement is not isolated, as it occurred concurrently with precipitate refinement. However, the findings of Figs. 3 and 9 show that grain refinement is correlated with increased corrosion rate.

The effects of crystallographic texture on corrosion rates were also difficult to isolate. Generally, studies have shown that grains with their basal plane exposed to the electrolyte exhibit lower corrosion rates than grains which expose the other HCP planes [5,37]. This effect is attributed to the basal plane being the least thermodynamically reactive, with the highest binding energy and lowest surface energy [5]. In general, studies of texture effects on corrosion rates for Mg alloys remain scarce in the literature. In the present study, the pole figures (Fig. 3) show that only two cases – ZKQX-AsRec's RD_0 plane and ZKQX-ECAP#3's FD plane – exposed primarily (0002) basal planes to the electrolyte during the corrosion testing. For the remaining six conditions, the $(10\bar{1}0)$ prismatic planes were primarily exposed to the electrolyte (Fig. 3). Because ZKQX-AsRec's RD_0 plane had a higher corrosion rate than its ED_0 plane (Fig. 9), corrosion rate appears more affected by differences in grain size or precipitate features than texture. In addition, while the ZKQX-ECAP#3's FD plane did not show a significantly lower corrosion rate than the other ECAP samples where the $(10\bar{1}0)$ planes were exposed to the electrolyte (Fig. 9). These findings demonstrate that texture effects on corrosion rate are seemingly minor for Mg alloys in comparison to grain size and precipitate effects.

Of the effects of grain size, crystallographic texture, and precipitates on corrosion rate, the effects of precipitates are perhaps most relevant

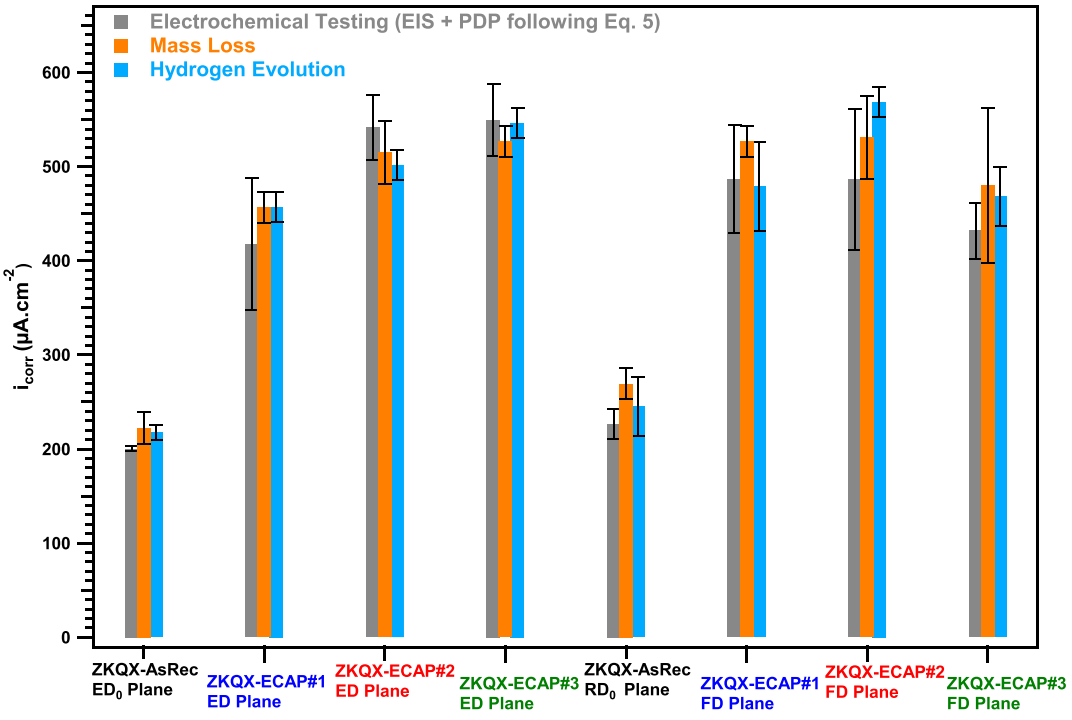

Fig. 9. Comparison of corrosion rates measured via mass loss, evolved hydrogen gas, and electrochemical experiments (Eq. (5)). General agreement across the different testing methods is evident. Here, the ZKQX-AsRec condition demonstrated the lowest corrosion current density, meaning that corrosion rate increases with ECAP processing for this material.

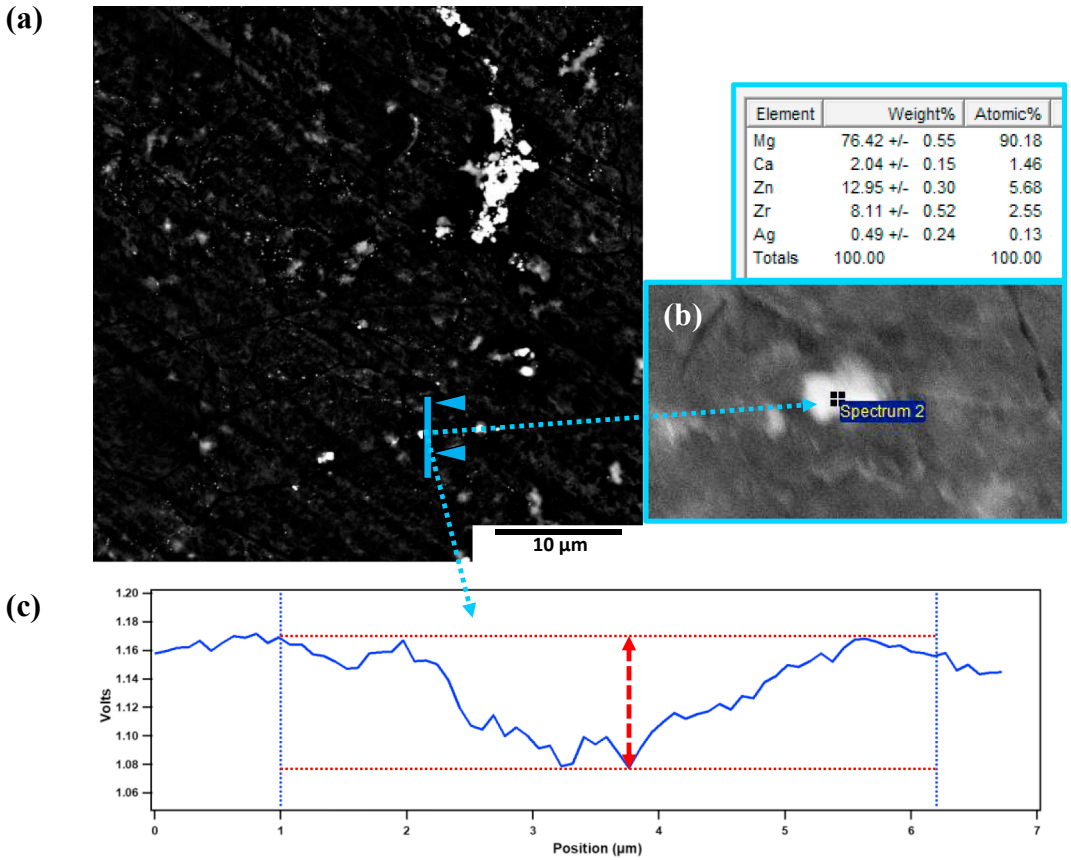

Fig. 10. (a) High contrast BSE image of the ED_0 plane of ZKQX-AsRec. Scanning kelvin probe force microscopy (SKPFM) was used to measure the potential along the region marked by the blue line, with measured potential values plotted in (c). The BSE/EDS results in (b) confirm the presence of a Zn-Zr enriched precipitate at the center of the SKPFM scan. Its chemistry is captured via EDS at location "Spectrum 2." The potential difference across the precipitate demonstrates that precipitates are cathodic to the Mg matrix, thereby enabling micro-galvanic corrosion. (For interpretation of the references to colour in this figure legend, the reader is referred to the web version of this article.)

as they are the most fundamental; that is, microgalvanic corrosion is a fundamental source for corrosion in all metals. To understand the effects of precipitates on corrosion rate, SKPFM was conducted on ZKQX-AsRec's ED_0 plane to determine the electrical potential between the matrix and precipitates. These results are shown in Fig. 10a–c. The electrical potential was measured at a precipitate relative to the surrounding Mg matrix in Fig. 10a. Here, the profile of this line scan is marked by the blue line, and its potential profile is plotted in Fig. 10c. Here, precipitates exhibit a difference of around 80 mV in potential vs. the Mg matrix. Note that the presence of a precipitate at the scanned area was verified via BSE in Fig. 10a–b; in Fig. 10b, an EDS scan reveals the precipitate to be Zn-Zr enriched. In essence, the SKPFM results shows that Zn-Zr enriched precipitates act as cathodic sites in the Mg-ZKQX6000 alloy. Therefore, these precipitates should accelerate corrosion rate.

In the absence of fine precipitates, corrosion rate seemingly reduces with large precipitates being more equiaxed, as seen when comparing corrosion rates (Fig. 9) and microstructural images (Figs. 3–5) of ZKQX-AsRec's ED_0 plane with its RD_0 plane. Figs. 3–5 also show clearly that ECAP heavily refined the cathodic Zn-Zr enriched precipitates. From the corrosion rates of Fig. 9, precipitate refinement is strongly correlated with increased corrosion rate. The increased corrosion rates with finer precipitates in ZKQX-ECAP#1–3 are a probable consequence of their cathodic nature [58,59] and their heterogeneous size, which is often too large to have a minimal effect on corrosion [30,60]. While Kim et al. [30] showed that nanometer sized cathodic precipitates in AZ61 showed less evidence of galvanic corrosion than larger precipitates, the precipitates in Figs. 3-5 are much larger than a few nanometers. Seong et al. [58] also demonstrated that finer *anodic* Mg_2Ca precipitates, being more disconnected, can allow for less uniform corrosion along grain boundaries, leading to reduced undercutting effects and improved corrosion resistance. Thus, the present findings show that nonuniform refinement of cathodic precipitates accelerate corrosion rate.

From the above findings, grain and precipitate refinement appears to detrimentally affect corrosion rate. To explain how this is happening, in-situ corrosion monitoring via a "drop test" was conducted for two samples, ZKQX-AsRec's RD_0 plane (Fig. 11) and the ZKQX-ECAP#3's FD plane (Fig. 12). Both conditions were chosen for comparison because they exhibited similar crystallographic textures (Fig. 3), serving to minimize texture effects while narrowing the focus to precipitate and grain size effects. Fig. 11a shows ZKQX-AsRec's RD_0 plane at the beginning of the drop test, when HBSS first wet the sample surface. Notice the large, oriented precipitates visible in Fig. 11a; these are Zn-Zr enriched (Fig. 5a) and are cathodic to the Mg matrix (Fig. 10). Fig. 11a–d shows, in chronological order, the effects of corrosion during the drop test. Here, times under HBSS are shown for each, and Fig. 11 shows that the Mg matrix corrodes first and is anodic relative to the precipitates, confirming findings from the SKPFM Volta potential measurements. In Fig. 11b, cathodic precipitates can be seen generating hydrogen gas. These hydrogen gas bubbles grew with time (Fig. 11c), eventually colliding and bursting (Fig. 11d), releasing hydrogen gas into the air. At the sites where hydrogen gas bubbles formed, pits were found (Fig. 11d). Fig. 11e shows the sample under optical microscope after the surface has dried, where pits and trenching underneath the precipitates can be seen. It appears that these pits form due to "trenching."

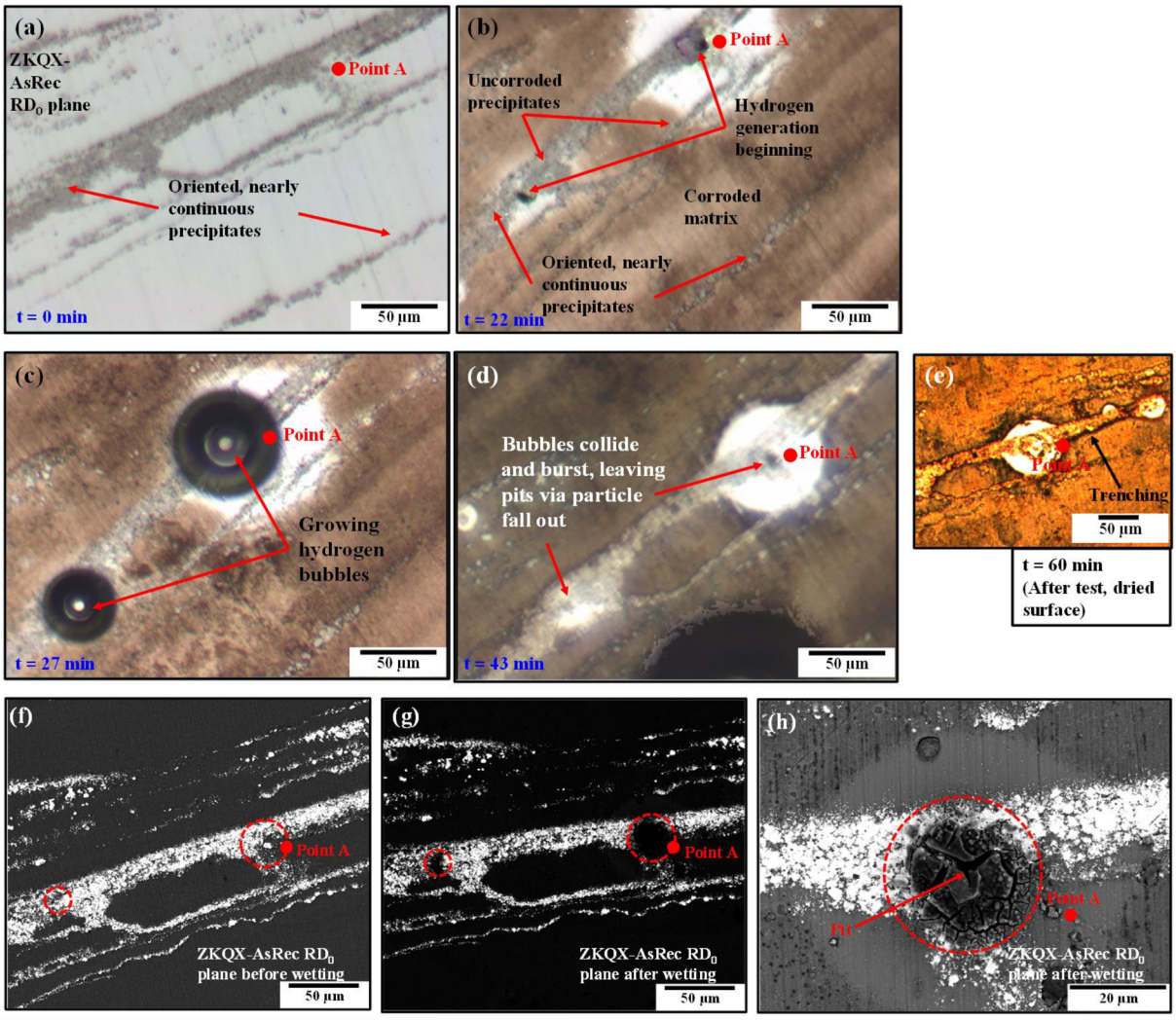

Fig. 11. (a–d) Chronological drop test images from the ZKQX-AsRec RD_0 plane showing the anodic matrix being preferentially attacked by corrosion. The formation of a hydrogen gas and pits, created via particle fall-out, can be seen. (e) shows trenching at the precipitate-matrix interface. (f–h) show BSE images, with (f) showing the sample before and (g-h) showing the sample after the drop test. Here, dashed red circles show where hydrogen gas bubbles were evolved and pits were formed. Point A marks the same position throughout the images as a reference point. (For interpretation of the references to colour in this figure legend, the reader is referred to the web version of this article.)

Trenching refers to the phenomenon where the Mg matrix beneath the cathodic precipitates completely corrodes away, undercutting the precipitate above it and allowing it to fall out. Fig. 11f shows via BSE the ZKQX-AsRec RD_0 plane prior to the drop test, and Fig. 11g–h show it afterwards. Here, particle fall-out occurred at the two red circles where hydrogen gas had evolved. Point A is marked for all images of Fig. 11 and serves as a reference point.

Overall, Fig. 11 shows that corrosion occurs preferentially at the Mg matrix adjacent to the cathodic precipitates, which can lead to trenching and pitting effects where particle fall-out may occur and expedite corrosion rate. While only precipitates in two areas were shown to experience particle fall-out, particle fall-out should eventually occur for the other regions as well. From Fig. 11a–d, the electrolyte evenly corrodes the Mg matrix, which uniformly darkens with time. While the grain boundaries are not visible, the fairly uniform corrosion here indicates that grain boundaries and sizes had a small effect on corrosion rate.

In comparison, Fig. 12a–d shows, in chronological order, the effects of corrosion during the drop test for ZKQX-ECAP#3's FD plane. Fig. 12e, g show the same surface via BSE and SE, respectively, before the drop test, while Fig. 12f, h show it afterwards. Point B is marked for all images of Fig. 12 and serves as a reference point. From Fig. 12e and g, the initial surface before corrosion had both dense precipitate regions and less dense precipitate regions, although in Fig. 12a, only the larger precipitates are clearly visible. Soon after wetting the surface with HBSS, anodic dissolution of the matrix occurred, as hydrogen gas bubbles once again evolved at cathodic precipitates (Fig. 12b–c). As the test proceeded, the surface began to show two distinct types of regions – one being dense with fine precipitates and another being less dense with these precipitates (Fig. 12c). In the regions dense with fine precipitates, corrosion occurred first, as indicated by its darker surface; in the less dense precipitate region, corrosion was less severe, as indicated by its lighter surface. Over time, both regions became darker as corrosion proceeded (Fig. 12d). The preferential corrosion at dense precipitate regions is confirmed from the SE images before and after the drop test (Fig. 12g–h), where dense precipitate region appears rougher than the less dense precipitate regions after corroding. Overall, corrosion occurred preferentially at regions containing refined precipitates and grains, probably due to the prevalence of micro-galvanic coupling in these regions. It also appears that the less-dense precipitate regions consist of larger grains which have relatively avoided refinement during ECAP. Therefore, the increased corrosion rate after ECAP may be

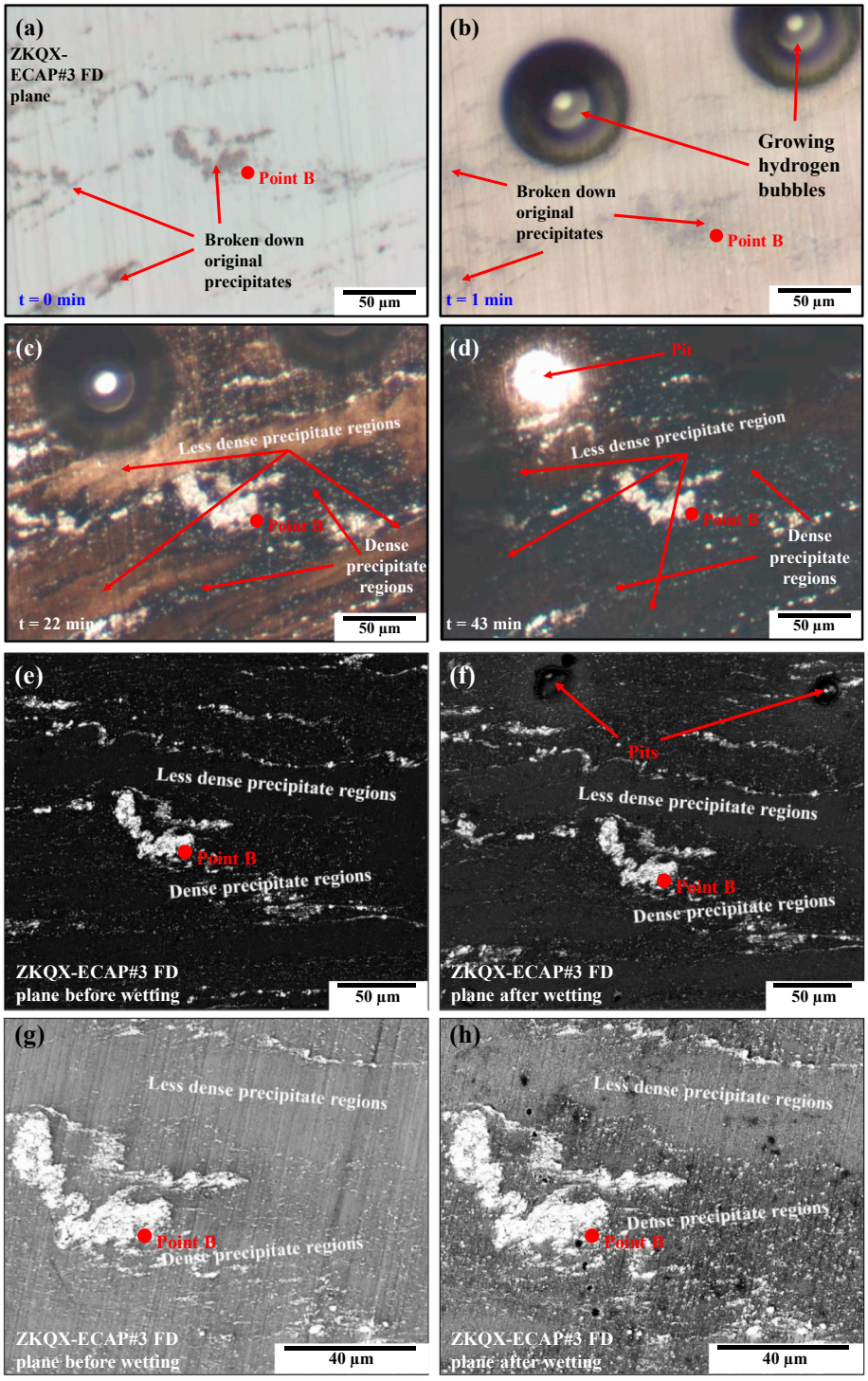

Fig. 12. (a–d) Chronological drop test images for testing the ZKQX-ECAP#3 FD plane. Here, corrosion occurs preferentially at the dense precipitate regions. (e, f) are BSE and (g, h) are SE images of the same region observed in (a–d), before (e, g) and after (f, h) the drop test. Corrosion occurred preferentially along the dense precipitate regions. Point B marks the same position throughout the images as a reference point.

influenced by these regions, which can act as cathodic sites relative to the heavily deformed sheared regions, where grains and precipitates have been refined. A higher corrosion rate for sheared regions is plausible, as dynamic precipitation [26], grain refinement [51], and higher dislocation densities [25] are known to occur at shear zones, making them more susceptible to corrosion attack.

The findings from the in-situ corrosion monitoring (Figs. 11–12) indicate that ECAP, while enhancing mechanical properties, detrimentally influenced corrosion resistance for the ZKQX6000 alloy via precipitate refinement and microgalvanic coupling. The mechanism for corrosion before and after ECAP is illustrated in Fig. 13. In Fig. 13a, precipitates are large prior to ECAP, and corrosion of the Mg matrix proceeds slowly and uniformly, expedited somewhat by pitting, particle fall-out, and trenching effects. In contrast, after ECAP (Fig. 13b), precipitates are much more refined. Here, corrosion of the Mg matrix occurs non-uniformly, preferentially attacking regions with refined grains and precipitates (i.e. the shear zones). While the corrosion effects of pitting and trenching continue as before, these effects can induce

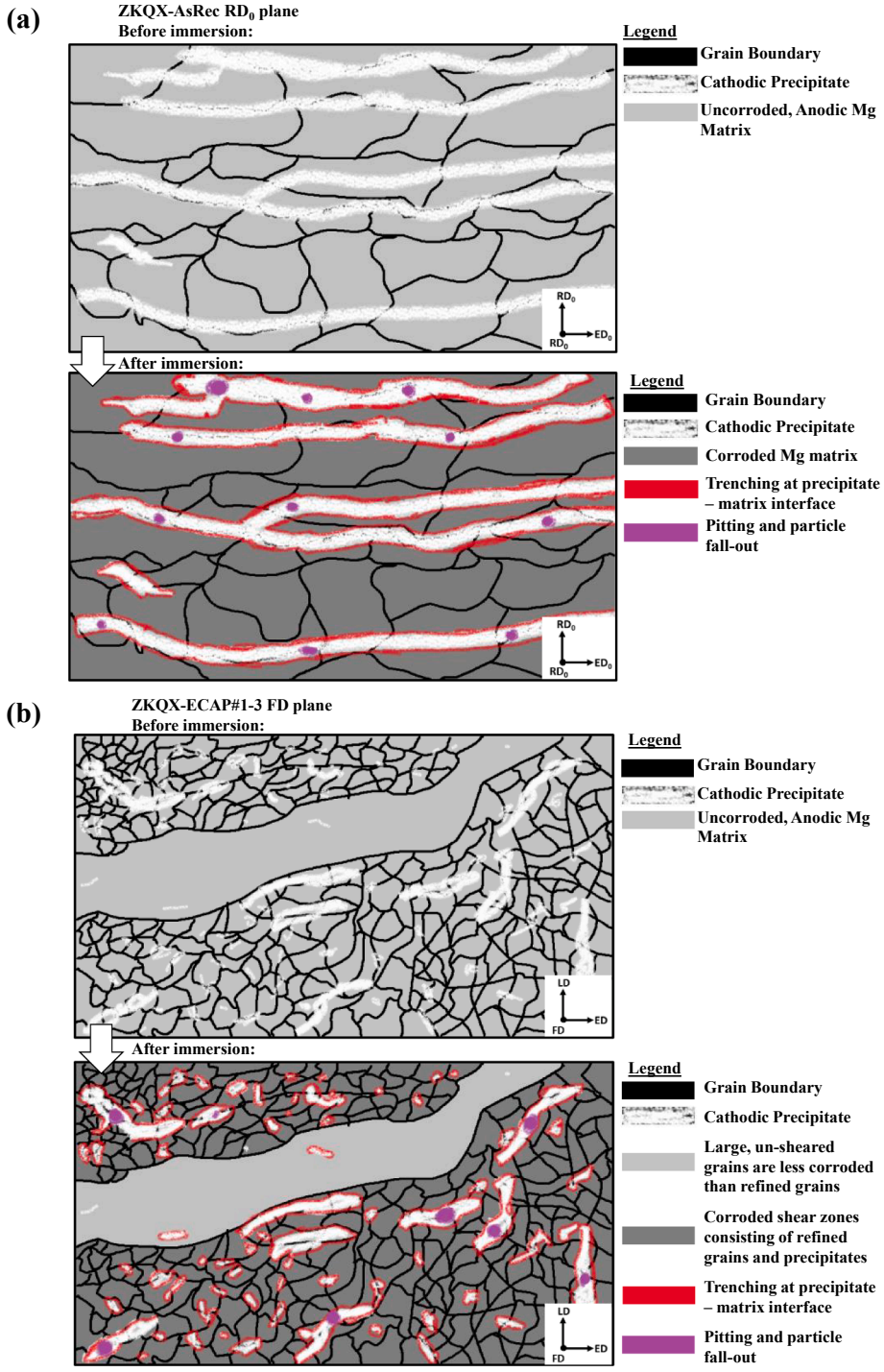

Fig. 13. Schematic illustrating the corrosion mechanisms for (a) the ZKQX-AsRec conditions and (b) the ZKQX-ECAP#1–3 conditions. In (a), corrosion occurs uniformly for the Mg matrix, being expedited somewhat due to precipitate trenching and particle fall-out. In (b), corrosion occurs more rapidly; the same effects of precipitate trenching and particle fall-out contribute to corrosion. However, large, less deformed and un-recrystallized grains also acted as cathodic regions to the shear zones, expediting corrosion. As precipitates are refined in case (b), precipitate fall-out and trenching can occur more rapidly as well.

particle fall-out more quickly because precipitates are more numerous and finer after ECAP. Likewise, this process ultimately increases the dissolution rate of the Mg matrix. As a result, a faster corrosion rate occurs after ECAP for the Mg-ZKQX6000 alloy.

4. Conclusions

The findings of present study on the effects of severe plastic deformation on the mechanical and corrosion properties of the Mg-ZKQX6000 alloy are summarized as follows:

1) Severe plastic deformation via ECAP produced high strength levels via the Hall-Petch effect. Samples with refined grain sizes of approximately 500 nm resulted in ultra-high UTS levels of nearly 400 MPa and UCS levels exceeding 500 MPa for several conditions. Optimal mechanical strengthening and ductility was inhibited by precipitate embrittlement effects and inhomogeneous microstructural refinement due partially to the unique hybrid ECAP routes

chosen.

2) ZKQX-ECAP#1–3 consistently showed a higher corrosion rate than ZKQX-AsRec in the electrolyte consistently buffered to a physiological pH of 7.4. For all conditions, corrosion was fairly rapid for Mg alloys. Corrosion rate calculations were shown to be consistent across mass loss, evolved hydrogen gas, and electrochemical testing methods.
3) ECAP of the ZKQX6000 alloy via unique hybrid routes caused precipitate refinement and grain refinement at dense sheared regions, yet did not homogeneously refine the microstructure. Rather, sheared regions of refined precipitates and grains corroded preferentially to the less dense precipitate regions, as seen via in-situ corrosion monitoring. Precipitate refinement appears to cause increased corrosion rate due to accelerated microgalvanic coupling. As the precipitate refinement occurred preferentially along shear zones, shear zones also detrimentally affected corrosion resistance.
4) For optimal viability of Mg alloys as orthopedic implant materials, the following suggestions are made from the present findings for future parallel studies on the design and thermomechanical processing of new Mg alloys for bioresorbable orthopedic implants:
   a. In vitro testing at physiological pH levels presents an essentially unforgiving corrosive environment challenge for Mg and its alloys. For optimal performance, therefore, alloys with minimal sources of corrosion are essential. Alloy design must strongly emphasize the minimization of cathodic precipitates along with selection of thermomechanical processing techniques that promote homogeneous, single phase microstructures for the best control over corrosion rates and mechanical properties.
   b. New Mg alloys would benefit from utilizing a conservative amount (ideally < 4 wt%) of alloying additions, in order to enable their complete placement into solid solution. The effects of ECAP on Mg alloys under complete solid solution merits further study.
   c. Zr and Zn should not be used together as alloying elements in Mg alloys for these applications, as the Zr reacted with Zn to form Zn-Zr enriched second phases that were difficult to place into solid solution, even after an extended (48 h) solution heat treatment. The effects of alloying on insoluble intermetallic phases merits further investigation.

CRediT authorship contribution statement

M.W. Vaughan: Investigation, Writing - original draft, Writing - review & editing, Visualization, Formal analysis. **A.I. Karayan:** Investigation, Writing - original draft, Visualization, Formal analysis. **A. Srivastava**: Investigation. **B. Mansoor**: Methodology, Formal analysis, Writing - review & editing, Supervision, Project administration, Funding acquisition. **J.M. Seitz:** Conceptualization, Resources, Funding acquisition. **R. Eifler:** Conceptualization, Resources, Funding acquisition. **I. Karaman**: Methodology, Formal analysis, Supervision, Project administration, Funding acquisition. **H. Castaneda**: Conceptualization, Resources, Supervision, Project administration. **H.J. Maier**: Conceptualization, Methodology, Resources, Funding acquisition.

Declaration of competing interest

The authors declare that they have no known competing financial interests or personal relationships that could have appeared to influence the work reported in this paper.

Acknowledgements

This publication was made possible by a National Priorities Research Program grant, NPRP 8-856-2-364 from the Qatar National Research Fund (a member of The Qatar Foundation). The statements made herein are solely the responsibility of the authors. MWV and IK acknowledge the financial support from the U.S. National Science Foundation under Grant Number CMMI-1563580 (Program Director: Dr. Alexis Lewis). HJM, JMS, and RE acknowledges the financial support from Deutsche Forschungsgemeinschaft (grant No. MA 1175/52-1). The technical assistance of Mr. Robert Barber, Mr. Michael Elverud, Dr. Christian Klose, and Dr. Marcus Engelhardt is much appreciated. Open Access funding provided by the Qatar National Library.

References

[1] J.-F. Nie, Metall. Mat. Trans. A 43 (2012) 3891–3939.
[2] C.L. Mendis, K. Oh-ishi, Y. Kawamura, T. Honma, S. Kamado, K. Hono, Acta Mater. 57 (2009) 749–760.
[3] C.L. Mendis, K. Oh-ishi, K. Hono, Scr. Mater. 57 (2007) 485–488.
[4] G.L. Song, A. Atrens, Adv. Eng. Mater. 1 (1999) 11–33.
[5] A. Atrens, G.-L. Song, M. Liu, Z. Shi, F. Cao, M.S. Dargusch, Adv. Eng. Mater. (2015) 400–453.
[6] S.N. Mathaudhu, E.A. Nyberg, Essential Readings in Magnesium Technology, (2016), pp. 71–76.
[7] H. Wang, Y. Estrin, H. Fu, G. Song, Z. Zúberová, Adv. Eng. Mater. 9 (2007) 967–972.
[8] S.M. Razavi, D.C. Foley, I. Karaman, K.T. Hartwig, O. Duygulu, L.J. Kecskes, S.N. Mathaudhu, V.H. Hammond, Scr. Mater. 67 (2012) 439–442.
[9] M. Vaughan, W. Nasim, E. Dogan, J. Herrington, G. Proust, A. Benzerga, I. Karaman, Acta Mater. 168 (2019) 448–472.
[10] I.J. Polmear, Light Alloys, Metallurgy of the Light Metals, Edward Arnold, London, 1995.
[11] D. Orlov, K.D. Ralston, N. Birbilis, Y. Estrin, Acta Mater. 59 (2011) 6176–6186.
[12] Y. Chen, Z. Xu, C. Smith, J. Sankar, Acta Biomater. 10 (2014) 4561–4573.
[13] J.-M. Seitz, A. Lucas, M. Kirschner, JOM 68 (2016) 1177–1182.
[14] F. Witte, N. Hort, C. Vogt, S. Cohen, K.U. Kainer, R. Willumeit, F. Feyerabend, Curr. Opinion Solid State Mater. Sci. 12 (2008) 63–72.
[15] Y. Ding, C. Wen, P. Hodgson, Y. Li, J. Mater. Chem. B 2 (2014) 1912–1933.
[16] X. Li, X. Liu, S. Wu, K. Yeung, Y. Zheng, P.K. Chu, Acta Biomater. 45 (2016) 2–30.
[17] H. Kalb, A. Rzany, B. Hensel, Corros. Sci. 57 (2012) 122–130.
[18] N. Kirkland, N. Birbilis, M. Staiger, Acta Biomater. 8 (2012) 925–936.
[19] G. Song, A. Atrens, Adv. Eng. Mater. 5 (2003) 837–858.
[20] J.M. Seitz, R. Eifler, F. Bach, H. Maier, J. Biomed. Mater. Res. A 102 (2014) 3744–3753.
[21] M.P. Staiger, A.M. Pietak, J. Huadmai, G. Dias, Biomaterials 27 (2006) 1728–1734.
[22] K. Gusieva, C. Davies, J. Scully, N. Birbilis, Int. Mater. Rev. 60 (2015) 169–194.
[23] E. Dogan, I. Karaman, G. Ayoub, G. Kridli, Mater. Sci. Eng. A 610 (2014) 220–227.
[24] D.C. Foley, M. Al-Maharbi, K.T. Hartwig, I. Karaman, L.J. Kecskes, S.N. Mathaudhu, Scr. Mater. 64 (2011) 193–196.
[25] D. Song, A. Ma, J. Jiang, P. Lin, D. Yang, J. Fan, Corros. Sci. 52 (2010) 481–490.
[26] E. Dogan, S. Wang, M.W. Vaughan, I. Karaman, Acta Mater. 116 (2016) 1–13.
[27] E. McCafferty, Introduction to Corrosion Science, Springer Science & Business Media, 2010.
[28] C.o.t. Hoog, N. Birbilis, Y. Estrin, Adv. Eng. Mater. 10 (2008) 579–582.
[29] N. Birbilis, K.D. Ralston, S. Virtanen, H.L. Fraser, C.H.J. Davies, Corros. Eng. Sci. Technol. 45 (2013) 224–230.
[30] H.S. Kim, W.J. Kim, Corros. Sci. 75 (2013) 228–238.
[31] N.N. Aung, W. Zhou, Corros. Sci. 52 (2010) 589–594.
[32] D. Song, A.B. Ma, J.H. Jiang, P.H. Lin, D.H. Yang, J.F. Fan, Corros. Sci. 53 (2011) 362–373.
[33] G.B. Hamu, D. Eliezer, L. Wagner, J. Alloys Compd. 468 (2009) 222–229.
[34] N. Martynenko, E. Lukyanova, V. Serebryany, D. Prosvirnin, V. Terentiev, G. Raab, S. Dobatkin, Y. Estrin, Mater. Lett. 238 (2019) 218–221.
[35] D. Song, C. Li, N. Liang, F. Yang, J. Jiang, J. Sun, G. Wu, A. Ma, X. Ma, Mater. Des. 166 (2019) 107621.
[36] G.-L. Song, JOM 64 (2012) 671–679.
[37] G.-L. Song, Z. Xu, Corros. Sci. 63 (2012) 100–112.
[38] R.Z. Valiev, T.G. Langdon, Prog. Mater. Sci. 51 (2006) 881–981.
[39] A. Yamashita, Z. Horita, T.G. Langdon, Mater. Sci. Eng. A 300 (2001) 142–147.
[40] E.O. Hall, Proc. Phys. Soc. B 64 (1951) 747.
[41] N.J. Petch, J. Iron Steel Inst. 174 (1953) 25–28.
[42] D. Tie, F. Feyerabend, W.-D. Mueller, R. Schade, K. Liefeith, K.U. Kainer, R. Willumeit, Eur. Cells Mater. 25 (2013) 284–298.
[43] Z. Liu, R. Schade, B. Luthringer, N. Hort, H. Rothe, S. Müller, K. Liefeith, R. Willumeit-Römer, F. Feyerabend, Oxidative Med. Cell. Longev. Volume 2017 (2017) 1–14.
[44] K. Jähn, H. Saito, H. Taipaleenmäki, A. Gasser, N. Hort, F. Feyerabend, H. Schlüter, J.M. Rueger, W. Lehmann, R. Willumeit-Römer, Acta Biomater. 36 (2016) 350–360.
[45] R.E. Barber, T. Dudo, P.B. Yasskin, K.T. Hartwig, Scr. Mater. 51 (2004) 373–377.
[46] A. King, N. Birbilis, J. Scully, Electrochim. Acta 121 (2014) 394–406.
[47] R.G. Kelly, J.R. Scully, D. Shoesmith, R.G. Buchheit, Electrochemical Techniques in Corrosion Science and Engineering, CRC Press, 2002.
[48] P. Karpuz, Ph.D. dissertation, Texas A&M University, 2012.
[49] M. Lentz, A. Behringer, C. Fahrenson, I. Beyerlein, W. Reimers, Metall. Mat. Trans. A 45 (2014) 4737–4741.

[50] M.R. Barnett, N. Stanford, P. Cizek, A. Beer, Z. Xuebin, Z. Keshavarz, JOM 61 (2009) 19–24.
[51] E. Dogan, M.W. Vaughan, S.J. Wang, I. Karaman, G. Proust, Acta Mater. 89 (2015) 408–422.
[52] A.K. Rodriguez, G.A. Ayoub, B. Mansoor, A.A. Benzerga, Acta Mater. 112 (2016) 194–208.
[53] M.W. Vaughan, J.M. Seitz, R. Eifler, H.J. Maier, I. Karaman, Magnesium Technology, (2017), pp. 43–51.
[54] Z. Shi, M. Liu, A. Atrens, Corros. Sci. 52 (2010) 579–588.
[55] J. Liao, M. Hotta, N. Yamamoto, Corros. Sci. 61 (2012) 208–214.
[56] K. Ralston, N. Birbilis, Corrosion 66 (2010) 075005–075005-075013.
[57] G.-L. Song, Z. Xu, Electrochim. Acta 55 (2010) 4148–4161.
[58] J.W. Seong, W.J. Kim, Acta Biomater. 11 (2015) 531–542.
[59] Y. Jeong, W. Kim, Corros. Sci. 82 (2014) 392–403.
[60] K. Ralston, N. Birbilis, M. Weyland, C. Hutchinson, Acta Mater. 58 (2010) 5941–5948.